

# Modelling stellar activity with Gaussian process regression networks

J. D. Camacho,<sup>1,2</sup>★ J. P. Faria,<sup>1,2</sup> P. T. P. Viana,<sup>1,2</sup>

<sup>1</sup> Instituto de Astrofísica e Ciências do Espaço, Universidade do Porto, Rua das Estrelas, 4150-762, Porto, Portugal

<sup>2</sup> Departamento de Física e Astronomia, Faculdade de Ciências, Universidade do Porto, Rua do Campo Alegre, 4169-007, Porto, Portugal

Accepted XXX. Received YYY; in original form ZZZ

## ABSTRACT

Stellar photospheric activity is known to limit the detection and characterisation of extra-solar planets. In particular, the study of Earth-like planets around Sun-like stars requires data analysis methods that can accurately model the stellar activity phenomena affecting radial velocity (RV) measurements. Gaussian Process Regression Networks (GPRNs) offer a principled approach to the analysis of simultaneous time-series, combining the structural properties of Bayesian neural networks with the non-parametric flexibility of Gaussian Processes. Using HARPS-N solar spectroscopic observations encompassing three years, we demonstrate that this framework is capable of jointly modelling RV data and traditional stellar activity indicators. Although we consider only the simplest GPRN configuration, we are able to describe the behaviour of solar RV data at least as accurately as previously published methods. We confirm the correlation between the RV and stellar activity time series reaches a maximum at separations of a few days, and find evidence of non-stationary behaviour in the time series, associated with an approaching solar activity minimum.

**Key words:** methods: data analysis – techniques: radial velocities – stars: individual: Sun

## 1 INTRODUCTION

The detection of extra-solar planets, henceforth exoplanets, as a research field in Astronomy started to develop from the discovery of 51 Pegasi *b* by Mayor & Queloz (1995). After the identification of this hot-Jupiter, many more followed with over 5000 exoplanets found so far. The two most successful techniques to detect exoplanets are the radial velocity (RV) and transit methods. The former relies on the fact that both planet and star orbit a common centre of mass, which generates a Doppler shift in the spectrum of the star that can be detected by high precision spectrographs.

Unfortunately, the use of RV data to detect and characterise exoplanets is not without its challenges. In particular, stellar magnetic activity is known to impact the RV measurements, imitating and/or hiding planetary signals (e.g. Figueira et al. 2010; Santos et al. 2010, 2014). Several activity indicators are commonly used to disentangle the activity and planetary signals present in the RVs, aiding the identification of periodic signals as stellar or planetary in origin (e.g. Figueira et al. 2013). More recently, the use of Gaussian processes (GP, Rasmussen & Williams 2006) has proved to be a successful tool to model RV data. While the GP covariance function describes the behaviour of the stellar RV contribution, the mean function is assumed to be generated by whatever planetary signals may be present (e.g. Haywood et al. 2014; Faria et al. 2016; Cloutier et al. 2019).

A new generation of spectrographs, e.g. EXPRES (Petersburg

et al. 2020) and ESPRESSO (Pepe et al. 2021), is providing RV measurements precise enough to enable the detection of Earth-like planets orbiting in the habitable zone of Sun-like stars. However, such planets cause a RV signal of the order of 10 cm/s, easily overwhelmed by the impact of stellar activity. Advanced statistical methods capable of characterising such feeble planetary signals are thus required. In this paper, we use a Gaussian process regression network (GPRN) to analyse solar RV data together with activity indicators, such as the full width at half maximum (FWHM) and the  $\log R'_{HK}$  index, and show that this framework can successfully describe the impact of stellar activity on RV data.

We start by introducing, in section 2, the challenges that stellar activity brings to exoplanet detection with RVs and with the definition of the main activity indicators used to identify stellar activity signals. In section 3, we present the GPRN framework, followed by some tests with simulated data in section 4. We describe the HARPS-N solar observations and interpret the results from applying the GPRN in section 5. Finally, section 6 presents a discussion and our conclusions.

## 2 THE STELLAR ACTIVITY RV IMPRINT

Stellar photospheric phenomena span a wide range of characteristic timescales, thus requiring different strategies in order for its impact to be addressed. Namely,

- on the timescale of a few minutes, pressure waves (p-modes) lead to the contraction and dilation of the stellar external envelope,

★ E-mail: joao.camacho@astro.up.pt

inducing RV signals of the order of 1 m/s (Schrijver & Zwaan 2000; Bazot et al. 2007);

- within a timescale of minutes to hours, granulation and supergranulation phenomena caused by convection in the external layers of solar-type stars induce signals with RV amplitudes also in the range of 1 m/s (Kjeldsen et al. 2008; Meunier & Lagrange 2019);
- due to the variation of the stellar radius, gravitational red-shift induces variations in the RV measurements of the order of a few cm/s (Cegla et al. 2012);
- magnetic activity related to spots, faculae, and plages induces quasi-periodic signals with amplitudes between 1 and 50 m/s, depending on the activity level and age of the stars (Saar & Donahue 1997; Santos et al. 2010; Lagrange et al. 2010), and characteristic periodicities ranging from the stellar rotation period up to the magnetic cycle, i.e. from days to years (Saar & Donahue 1997; Baliunas et al. 1995).

The RV impact of pressure waves and the different types of granulation can be addressed, at least in part, using specific observational strategies (e.g. Dumusque et al. 2011). But the activity signals induced by active regions need to be modelled, since they encompass the most interesting range of orbital periods from an habitability point of view, and are known to hide or mimic planetary signals in RV measurements (e.g. Robertson et al. 2014; Santos et al. 2014; Guinan et al. 2016).

However, the joint identification and characterisation of the complex RV signals induced by stellar magnetic activity and those due to orbiting planets is often challenging. One way to tackle this issue is by using the information contained in line-profile or chromospheric activity indicators, which by construction should not be affected by any orbiting planets. In this work, we focus on three such indicators, the FWHM, the BIS, and the  $\log R'_{HK}$  index (see, e.g., Figueira et al. 2013; Gomes da Silva et al. 2012). These are estimated jointly with the RVs through analysis of the cross-correlation function (CCF) and the Calcium H and K lines.

Nevertheless, our framework is general enough to accommodate any number of activity proxies which are observed simultaneously with the RVs. For example, stellar magnetic activity also affects photometric observations and high-precision photometry has been used as a proxy when characterising planet signals in RV data (e.g. Haywood et al. 2014; Kosiarek & Crossfield 2020). Yet, as it is currently implemented (see section 3), the GPRN requires that all time-series have equal timestamps, which precludes the use of non-simultaneous photometric observations, even if they are contemporaneous. This limitation may be addressed in future work.

### 3 GAUSSIAN PROCESS REGRESSION NETWORKS

In a seminal paper, Rajpaul et al. (2015) proposed a framework to jointly model RVs and several activity indicators. The key insight was to extend the FF' method from Aigrain et al. (2012), which relates the activity signal expected in the RVs to the relative drop in flux caused by point-like spots (denoted F) and its first time derivative. From this premise, Rajpaul et al. (2015) modelled F with a latent Gaussian Process (GP) and derived the necessary expressions for a multi-output model based on linear combinations of F and F'. They used the  $\log R'_{HK}$  and the BIS because of their sensitivity to the spot coverage on the star.

More recently, Barragán et al. (2021) extended this approach to a more general set of activity indicators and presented an efficient implementation within the `pyaneti` package (Barragán et al. 2019a). The framework has also been extended by Jones et al.

(2017), who included terms proportional to the second time derivative of the latent GP and by Gilbertson et al. (2020), who developed the GLOM model allowing for the use of any covariance kernel. This methodology has proven useful in disentangling planetary and stellar induced signals in RV data with different levels of activity (e.g. Barragán et al. 2019b; Mayo et al. 2019).

While these approaches are an improvement with respect to the traditional GP regression framework that models only RVs, they are limited by their inability to tackle the non-stationary behaviour of stellar magnetic activity as a function of time (e.g. Demin et al. 2018), i.e. they are incapable of addressing processes whose characteristics vary across the input space (Plagemann et al. 2008). The development of a framework that combines the information present in activity indicators and is also capable of tackling non-stationary should thus help the identification of the RV component due to stellar activity and improve planet detection and characterisation. This was the motivation behind the implementation of a Gaussian process regression network (GPRN) framework as a means for the joint analysis of RV data and activity indicators.

#### 3.1 Gaussian processes

We first review the basic concepts behind a more traditional GP, which will also be useful for the presentation of the GPRN framework. In brief, a GP is a generalisation of the multivariate Gaussian distribution, characterised by a mean function  $m(t)$  and a covariance function  $k(t, t')$ , more commonly known as the *kernel*. More formally, a GP is a stochastic process with Gaussian marginal distributions, thus defining a distribution over functions, i.e. each draw from a GP represents a function (Quadrianto et al. 2010).

A GP is sufficiently flexible to model the quasi-periodic covariance structure induced by stellar activity in RV measurements, by means of its kernel, while also being able to take into account Keplerian contributions to the RVs through its mean function (e.g. Haywood et al. 2014; Faria et al. 2016; Cloutier et al. 2019). The most commonly used GP kernel in RV analysis is the quasi-periodic (QP) kernel, obtained from the multiplication of a periodic and a squared-exponential covariance function:

$$k_{QP}(t, t') = \eta_1^2 \exp \left[ -\frac{(t-t')^2}{2\eta_2^2} - \frac{2}{\eta_4} \sin^2 \left( \frac{\pi(t-t')}{\eta_3} \right) \right]. \quad (1)$$

The kernel hyper-parameters  $\eta$  can have a physical interpretation. While  $\eta_1$  relates to the strength of the correlation between RVs at different time separations,  $\eta_2$  and  $\eta_3$  reflect the evolution timescale of the active regions at the stellar surface and the stellar rotation period, respectively. Lastly,  $\eta_4$  controls how sinusoidal the GP latent functions are or, in other words, their timescale of variation relative to  $\eta_3$ . For smaller values of  $\eta_4$ , the functions will show more short-scale structure within one stellar rotation period (e.g. Rajpaul 2017).

With the mean and covariance functions defined and parameterised, the next step is to condition the GP on the observed data. We start by writing the log marginal likelihood of a set of observations  $y$  under the GP,

$$\log \mathcal{L} = -\frac{1}{2} \mathbf{r}^T \mathbf{K}^{-1} \mathbf{r} - \frac{1}{2} \log |\mathbf{K}| - \frac{n}{2} \log (2\pi), \quad (2)$$

where  $\mathbf{r}$  is the vector of residuals after subtraction of the mean function,  $\mathbf{K}$  the covariance matrix of the GP, and  $n$  the number of measurements. The three terms in Equation (2) can be interpreted as a measure of the goodness-of-fit, a penalisation for the complexity of the covariance function, and a normalisation constant, respectively (see Rasmussen & Williams 2006).

The marginal likelihood can be maximised to obtain a set of ‘best’ hyper-parameters compatible with the data. Alternatively, one can place prior distributions on each of the hyper-parameters (of the mean and covariance functions) and sample from their posterior distributions using, for example, MCMC. For this work, we explored several publicly available MCMC packages such as *emcee* (Foreman-Mackey et al. 2019), *dynesty* (Speagle 2020), and *zeus* (Karamanis et al. 2021), finally settling on *emcee*.

### 3.2 A GPRN model for stellar activity

Jointly modelling RVs and activity indicators can be framed as a multi-output regression problem. Generalising GPs for multi-output problems is not a trivial task, since the statistical dependence across the different datasets (or data *channels*) must be explicitly modelled. Here we explore GPRNs (Wilson et al. 2012) as a set of promising Bayesian models for multi-output regression which exploit the structural properties of neural networks and the flexibility of non-parametric function learning offered by GPs. As we will see, GPRNs can capture input-dependent, highly non-linear correlations between the outputs, provide heavy-tailed predictive distributions, and can resist over-fitting.

Following Wilson et al. (2012), we write the GPRN model for a set of  $P$  outputs  $y(t)$  as

$$y(t) = \mathbf{W}(t) [f(t) + \sigma_f \epsilon(t)] + \sigma_y z(t) \quad (3)$$

where we introduced a small set of  $Q$  latent functions (called *nodes*)  $f(t)$  and a  $P \times Q$  projection matrix  $\mathbf{W}(t)$  of *weight* functions. Both the nodes and the weights follow independent GP priors

$$f_j(t) \sim \mathcal{GP}(0, k_{f_j}) \text{ for } j = 1, \dots, Q, \quad (4)$$

$$W_{ij}(t) \sim \mathcal{GP}(0, k_{w_{ij}}) \text{ for } i = 1, \dots, P \text{ and } j = 1, \dots, Q \quad (5)$$

with zero means and kernels  $k_{f_j}$  and  $k_{w_{ij}}$ , respectively. In equation (3), both  $\epsilon(t)$  and  $z(t)$  are independent, white noise processes sampled from the standard normal distribution. We make the simplifying assumption of setting  $\sigma_f = 0$ , i.e. we assume a priori that the white noise component of the model is stationary, akin to a so-called jitter term. We associate one such term, characterised by its standard deviation  $\sigma_i$ , to each dataset  $i$ . However, we also have to take into account the independent measurement uncertainties that we know affect the data. Each measurement  $n$  in dataset  $i$  has an associated uncertainty described by a normal distribution with standard deviation  $\sigma_{i,n}$ . Therefore

$$\sigma_y \rightarrow \sigma_{y_i} = \sqrt{\sigma_i^2 + \sigma_{i,n}^2} \quad (6)$$

where each  $\sigma_{y_i}$  depends implicitly on  $n$ .

The overall structure of the GPRN creates a non-stationary linear combination of independent GPs. The correlations between the various variables are modelled by the latent functions  $f(t)$  (Nguyen & Bonilla 2013). The final amplitudes are given by projection through the weight functions  $\mathbf{W}(t)$ , making the correlations input dependent and resulting in non-stationary outputs (Heinonen et al. 2016).

In the simplest case the GPRN has two latent variables, one node and one weight, causing *a priori* the output to have a marginal distribution defined by the product of two independent Gaussian distributions. This product is not in general a Gaussian distribution but instead follows a re-normalised Bessel distribution of the second kind and order zero (e.g. Arfken et al. 2013; Cui et al. 2016), which has longer tails than a Gaussian. This will occur regardless of the type of covariance function used for the node and the weight GPs.

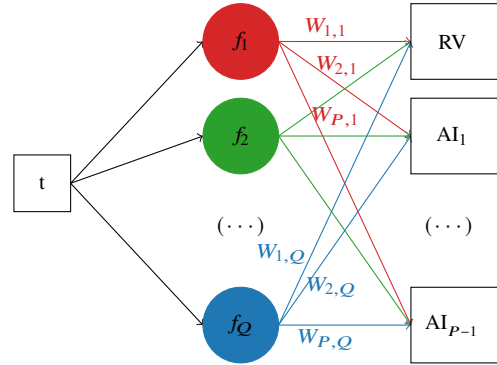


**Figure 1.** Diagram of a GPRN applied to  $p$  datasets consisting of RVs and  $p - 1$  activity indicators (AI). For example,  $AI_1$  could be the FWHM and  $AI_2$  the BIS. The regression network is formed by  $Q$  nodes  $[f_1(t), f_2(t), \dots, f_Q(t)]$  and  $P \times Q$  weights  $[W_{11}(t), \dots, W_{P1}(t), \dots, W_{1Q}(t), \dots, W_{PQ}(t)]$ . For simplicity, we dropped their dependence on  $t$  in the diagram, but each  $f$  and  $W$  follows an independent GP prior.

Thus, the GPRN posterior predictive distribution has the flexibility to be heavier-tailed than the (Gaussian) predictive of a GP, making it more robust with respect to the possible presence of outliers. This also implies that some popular goodness-of-fit metrics, like the root mean square (rms) residuals, should be applied with care to GPRN results, especially when comparing GPRN residuals to those from a GP.

The covariance functions for the latent GPs,  $f(t)$  and  $\mathbf{W}(t)$ , can take any form (periodic, quasi-periodic, squared exponential) and they can be shared among all nodes or all weights, or individually defined. This allows for a model with an overall covariance kernel that continuously shifts between regions with completely different covariance structures, thus accommodating non-stationary correlations in the outputs (Wilson 2014; Li et al. 2020). This suggests a GPRN can be used to model the complex, non-periodic signals with different decaying timescales and non-stationary amplitudes that are often the result of stellar activity.

In our application, we use the GPRN to model RVs together with  $P - 1$  stellar activity indicators (AI), with identical timestamps. This scheme is exemplified in the diagram of Figure 1. The main objective of this framework is to use the information contained in the activity indicators to help characterise better the impact of activity in the RVs, thus enabling a cleaner identification of any planetary signals that may be present. Again, each of the nodes and weights in Figure 1 are functions of time,  $t$ . This allows for a fit to the data that can accommodate deviations from the stationary expectation coming from a node. If the model incorporates several nodes, the time-varying weights make it possible for each node to have a different impact throughout the data.

Henceforth, we will only consider the simplest possible configuration for a GPRN, with just one node plus one weight per time series. Such a model should be capable of capturing the quasi-periodic behaviour of the active regions on the surface of a star with the node, while the weights describe the variations associated with a longer-term magnetic cycle. This GPRN configuration is also the closest possible to the GP framework used in many previous works, thus it constitutes a natural starting point for the exploration of the GPRN capabilities.

### 3.2.1 Variational inference

In contrast to a standard single-output GP, inference with a GPRN model is intractable due to the lack of analytical expressions for the joint posterior distribution with respect to the latent functions  $f(t)$  and  $\mathbf{W}(t)$ . In order to overcome this, [Wilson et al. \(2012\)](#) originally proposed two approaches based on variational Bayes and MCMC. [Nguyen & Bonilla \(2013\)](#) later developed more efficient methods based on variational inference ([Jordan et al. 1999](#)). Their aim was to find, among a family of factorised distributions, the closest approximating distribution  $q(\mathbf{f}, \mathbf{W})$  to the true posterior  $p(\mathbf{f}, \mathbf{W}|D)$ . The closeness of the approximation is measured through the Kullback-Leibler (KL, [Kullback 1959](#)) divergence between  $q(\mathbf{f}, \mathbf{W})$  and  $p(\mathbf{f}, \mathbf{W}|D)$ ,

$$\text{KL} [q(\mathbf{f}, \mathbf{W}) \parallel p(\mathbf{f}, \mathbf{W}|D)] = \mathbb{E} \left[ \log \frac{q(\mathbf{f}, \mathbf{W})}{p(\mathbf{f}, \mathbf{W}|D)} \right], \quad (7)$$

where  $\mathbb{E}$  stands for expectation or expected value. One particular family of factorised distributions is the so-called mean-field approximation, which takes the form

$$q(\mathbf{f}, \mathbf{W}) = \prod_{j=1}^Q q_f(f_j) \prod_{i=1}^P q_w(w_{ij}) \quad (8)$$

where  $q_f(f_j) = \mathcal{N}(\mu_{f_j}, \Sigma_{f_j})$  and  $q_w(w_{ij}) = \mathcal{N}(\mu_{w_{ij}}, \Sigma_{w_{ij}})$  are general Gaussian distributions. This factorisation allows for analytical, alternating updates for the variational parameters  $\mu$  and  $\Sigma$ , whose expressions are provided in [Appendix A](#).

Minimising the KL divergence in [equation \(7\)](#) is equivalent to maximising the evidence lower bound (ELBO, [Blei et al. 2017](#)), which for the GPRN is given by

$$\text{ELBO}(q) = \mathbb{E}_q [\log p(D|\mathbf{f}, \mathbf{W})] + \mathbb{E}_q [\log p(\mathbf{f}, \mathbf{W})] + \mathcal{H}_q [q(\mathbf{f}, \mathbf{W})], \quad (9)$$

where the first term is the expected log-likelihood, the second is the expected log-prior and the last is the entropy of  $q(\mathbf{f}, \mathbf{W})$ . For the full Gaussian mean-field approximation, presented in [expression \(8\)](#), the three terms in [equation \(9\)](#) can be computed in closed form. The expressions were provided by [Nguyen & Bonilla \(2013\)](#) and are reproduced in [Appendix B](#).

The expected values of the outputs  $i$  for a new input time  $t^*$  are also provided in [Nguyen & Bonilla \(2013\)](#). This so-called predictive mean for the outputs  $\mathbf{y}_i^*(t^*)$ , considering that the nodes and weights are independent, is given by

$$\begin{aligned} \mathbb{E} [\mathbf{y}_i^*(t^*)] &= \sum_{j=1}^Q \mathbb{E} [W_{ij}^*] \mathbb{E} [f_j^*] \\ &= \sum_{j=1}^Q K_{w_{ij}}^* K_{w_{ij}}^{-1} \mu_{w_{ij}} K_{f_j}^* K_{f_j}^{-1} \mu_{f_j}. \end{aligned} \quad (10)$$

In this equation the predictive mean for each  $\mathbf{y}_i^*(t^*)$  is obtained by summing the expected value of each node  $f_j$  multiplied by the expected value of the weight  $W_{ij}$  that connects  $f_j$  to  $y_i$ .

The predictive variances for the outputs  $i$  can be calculated through ([Wilson et al. 2012](#))

$$\begin{aligned} \mathbb{V} [\mathbf{y}_i^*(t^*)] &= \sum_{j=1}^Q \left[ \mathbb{E} [W_{ij}^*]^2 \mathbb{V} [f_j^*] \right. \\ &\quad \left. + \mathbb{V} [W_{ij}^*] \mathbb{E} [f_j^*]^2 \right] + \sigma_i^2, \end{aligned} \quad (11)$$

where  $\mathbb{V}$  stands for variance, with respect to either the node  $f_j$  or the weight  $W_{ij}$ , while  $\sigma_i$  is the jitter term mentioned in [equation 6](#). Note that this variance is with respect to the predictive outputs of the GPRN model, not the predictive values for a measurement made at  $t^*$ . Although the predictions are the same, the associated variance differs due to the extra uncertainty associated with the measurement process. In particular, the expression for the variance associated with the predictive values for the HARPS-N measurements made at the observed times differs from what is provided by [equation 11](#) insofar that instead of  $\sigma_i$  one should use  $\sigma_{y_i}$  as given by [equation 6](#).

We tested the implementation and accuracy of the mean-field approximation by comparing it with the MCMC approach proposed by [Wilson et al. \(2012\)](#), which relies on Elliptical Slice Sampling ([Murray et al. 2010](#)) to characterise the GPRN posterior. We found that both approaches provide fully compatible results for the predictive distributions. The MCMC algorithm is, however, much more computationally demanding.

The expressions for mean-field inference in the context of a GPRN, applied to RVs and activity indicators, were implemented in a Python package called `gpyrn`, that is made publicly available<sup>1</sup>. The implementation is computationally simple but could benefit from further optimisation to speed up some linear algebra calculations. The run-time is dominated by the inversion of  $N \times N$  covariance matrices for the node and weight GPs which, as currently implemented, scales with  $N^3$ . In principle, some of these calculations could use more scalable approaches such as those implemented in the `celerite` ([Foreman-Mackey et al. 2017](#)) or `S+LEAF` ([Delisle et al. 2022](#)) packages, for example. The results presented in [section 4](#) below were obtained on a standard laptop computer with an Intel<sup>®</sup> Core™ i7-6700HQ CPU, while for the more demanding analyses of [section 5](#) we used a computer cluster equipped with a 24-core Intel<sup>®</sup> Xeon<sup>®</sup> E5620 CPU.

## 4 APPLICATION TO SIMULATED DATA

In order to test the GPRN implementation, we simulated twenty sets of 50 observations each using a GPRN with one node and two different weights. The node was assumed to have a quasi-periodic covariance function, as given by [Equation 1](#), with an amplitude  $\eta_1^n = 1$  m/s, a decaying timescale  $\eta_2^n = 17$  days, a period  $\eta_3^n = 23$  days, and  $\eta_4^n = 0.75$ . Each weight was assumed to have a squared exponential covariance function,

$$k_{SE}(t, t') = \eta_1^2 \exp \left[ -\frac{(t-t')^2}{2\eta_2^2} \right], \quad (12)$$

with the same variance  $\eta_1^w = 7$  m/s, but different decaying timescales  $\eta_2^w$  of 29 days and 109 days. Both node and weights had mean functions equal to zero. Henceforth, the node and weight hyper-parameters are identified by the superscripts  $n$  and  $w$ , respectively.

The times for the observations were randomly drawn from an uniform distribution between 0 and 150 days. These input times are shared by both simulated datasets, whose outputs were obtained by multiplying one sample from the GP prior for the node with one independent sample from the GP prior for each weight. In order to make these outputs resemble more closely real observations, we added to each a simulated measurement error drawn from a normal distribution with mean equal to 0 m/s and standard deviation equal

<sup>1</sup> <https://github.com/iastr-pt/gpyrn>

Hyper-parameter	Description	Prior	Input	Units
$\eta_2^n$	Decaying timescale	$\mathcal{L}\mathcal{U}(\delta t_{\text{av}}, 10 t_{\text{span}})$	17	days
$\eta_3^n$	Period	$\mathcal{U}(10, 50)$	23	days
$\eta_4^n$	Lengthscale	$\mathcal{L}\mathcal{U}(0.1, 5)$	0.75	
$\eta_1^w$	Amplitude	$\mathcal{M}\mathcal{L}\mathcal{U}(y_\sigma, 2 y_{\text{ptp}})$	7	m/s
			7	m/s
$\eta_2^w$	Decaying timescale	$\mathcal{L}\mathcal{U}(\delta t_{\text{av}}, 10 t_{\text{span}})$	29	days
			109	days
s	White noise amplitude	$\mathcal{M}\mathcal{L}\mathcal{U}(y_\sigma, 2 y_{\text{ptp}})$	0	m/s
			0	m/s

**Table 1.** Hyper-parameter input values for the simulations, and assumed priors for the GPRN analysis of the simulated data. The superscripts on some hyper-parameters identify if they belong to the node ( $n$ ) or to the weights ( $w$ ). In the case of the prior distributions,  $\mathcal{U}(a, b)$  denotes a uniform distribution between  $a$  and  $b$ ,  $\mathcal{L}\mathcal{U}(a, b)$  a log-uniform distribution between  $a$  and  $b$ , while  $\mathcal{M}\mathcal{L}\mathcal{U}$  is a modified log-uniform distribution with *knee*  $a$  and upper limit  $b$  (see eqn. 16 in Gregory 2005). Also,  $\delta t_{\text{av}}$  is the average time between consecutive observations and  $t_{\text{span}}$  is the timespan of the observations, while  $y_\sigma$  and  $y_{\text{ptp}}$  are the standard deviation and peak-to-peak difference for a given vector of observations  $y$ , respectively. We fix the amplitude of the node,  $\eta_1^n$ , to 1 m/s.

to 1 m/s. Note that the GPRN model used in the simulation does not contain any white noise process, i.e. we set the jitter terms to zero, namely in equation 6.

We then analysed the simulated observations, expecting to recover, on average, the assumed values for the GPRN hyper-parameters as well as the latent functions. The GPRN model used in the analysis was the same as for the simulations, except that the weight variances  $\eta_1^w$  were assumed different and we included a free jitter hyper-parameter per dataset to account for possible Gaussian white noise. The uncertainties associated with the simulated measurements were assumed known a priori and added in quadrature to those jitter terms, as described through equation 6. In order to simplify the analysis, we fixed the mean functions to zero, and the amplitude of the node,  $\eta_1^n$ , to its fiducial value of 1 m/s. The prior distributions are listed in Table 1 and we use emcee (Foreman-Mackey et al. 2019) to characterise the posterior distribution for the model hyper-parameters. We set the number of MCMC walkers to twice the number of hyper-parameters and run the chains until a convergence criteria of 25 times the integrated autocorrelation time,  $\tau$ , is achieved. This criterion defines  $\tau$  as the number of steps needed for a chain to forget where it began or reach equilibrium (Sokal 1997). We calculated the value of  $\tau$  every 5000 iterations. We then discarded the  $2\tau$  initial samples as burn-in.

Figure 2 displays the results for one of the simulated datasets, showing the predictive means for the outputs, the node, and the weights assuming the MAP values for the GPRN hyper-parameters. As expected the GPRN manages to capture the structure of both time series and also of the latent node and weights. While for individual datasets the recovered hyper-parameters can deviate from the input values, the average results from the twenty simulations show no significant biases, except for the decaying timescales of both weights which tend to be overestimated. This suggests the node was capable of modelling some of the long-term variations present in the simulated data, leading to a relative increase in the posterior probability of large values for the timescales of the weights.

## 5 SUN AS A STAR OBSERVATIONS

The Sun has been continuously studied and monitored over millennia, enabling us to determine its characteristics with high precision.

It is a typical main-sequence star of spectral type G2V with a radiative interior and a convective shell (Del Zanna & Mason 2013). The solar dynamo is the physical process responsible for the magnetic activity that gives rise to the stellar signals that appear in RV measurements (e.g. Pagano 2013; Charbonneau 2014). The level of magnetic activity changes with time, leading to a 11-year sunspot cycle, during which the number of spots, flares and coronal mass ejections varies (see e.g. Hathaway 2015).

In this work, we analyse three years of Sun-as-a-star observations from the HARPS-N solar telescope (Dumusque et al. 2015). The observations were obtained between 2015 and 2018, during the declining phase of solar cycle 24. The data was first presented and analysed by Collier Cameron et al. (2019). More recently, Dumusque et al. (2021) re-visited the data after adapting the ESPRESSO DRS (Pepe et al. 2021) to the HARPS-N spectrograph, and re-estimated the solar RVs. They adopted a more stringent criteria to evaluate the quality of the individual spectra, obtaining a decrease in the day-to-day RV scatter and a stronger correlation between the RVs and activity indicators. The full set of spectra, CCFs, and RV time series are publicly available through the DACE platform<sup>2</sup>.

In total, there are 34550 RV measurements available. To simulate a standard 15-minute exposure for solar-type stars, which helps remove the RV contributions from oscillations and granulation, we randomly selected three consecutive measurements per day (when ever possible) and averaged them, discarding all other data points. The RV and  $\log R'_{HK}$  uncertainties were determined by adding quadratically the uncertainties for each set of three measurements, i.e. they were calculated by taking the square root of the average of these uncertainties squared and then dividing by three. The uncertainties associated with the BIS and FWHM averaged measurements were then defined as twice the value of the RV uncertainties. This leads to a total of 497 RV, FWHM, BIS, and  $\log R'_{HK}$  averaged measurements, spanning 1094 days (see Figure 3). Since the effects of the Solar System planets were already removed from the RVs, these time series can be assumed to contain only the imprint of solar activity, on timescales exceeding 15 minutes, and are thus an excellent test set for applying the GPRN.

<sup>2</sup> <https://dace.unige.ch/sun>

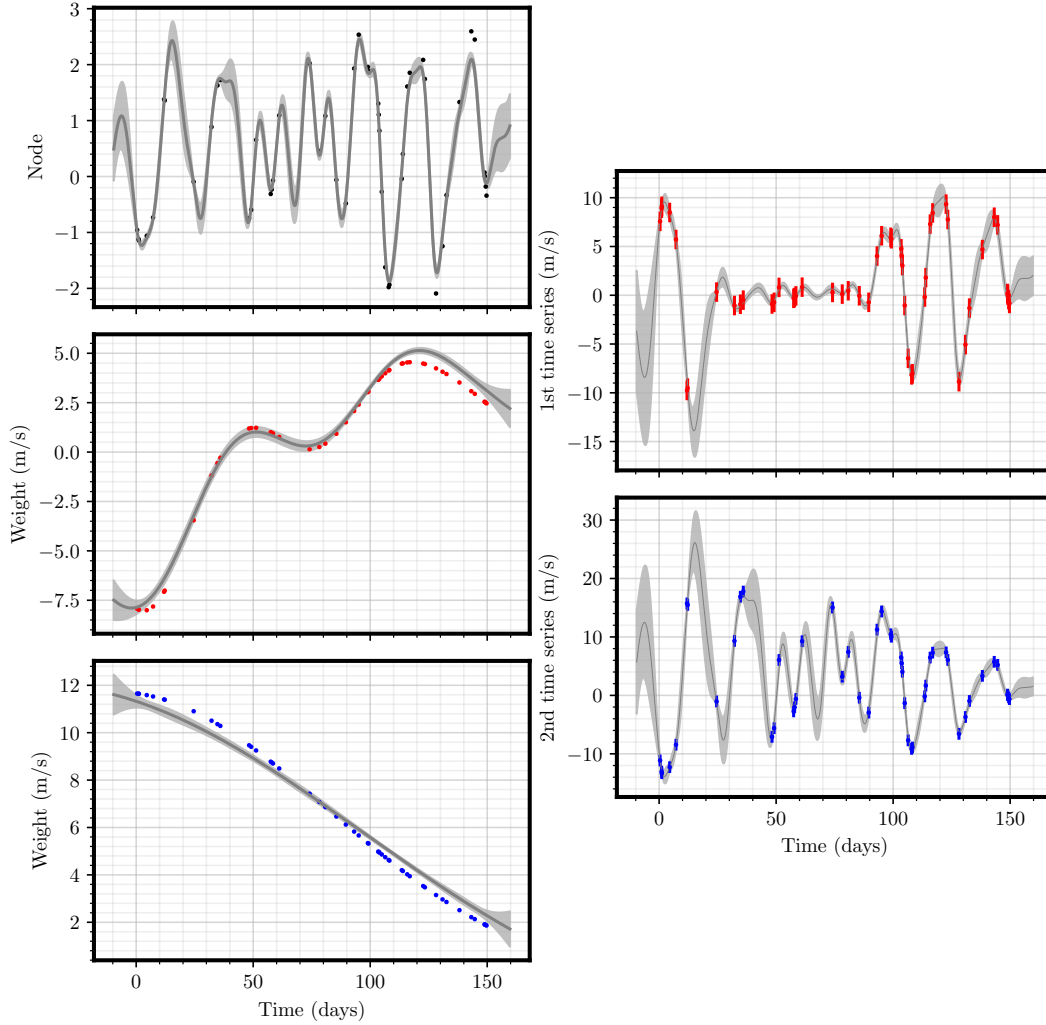


**Figure 2.** The left panels show the simulated values (dots) and the posterior predictive means (black lines) for the node and the weights connected to the first and second time series, assuming the inferred MAP values for the GPRN hyper-parameters. The grey band around each line represents the square root of the posterior predictive covariance. The right panels show the same quantities with respect to the simulated outputs, as well as the uncertainties associated with the later.

### 5.1 Periodogram analysis

We would like to check for the presence of periodic signals in the solar data before using the GPRN framework to analyse them. Thus, we computed the generalised Lomb-Scargle (GLS, [Zechmeister & Kürster 2009](#); [Astropy Collaboration et al. 2018](#)) periodogram for each of the assembled RV, BIS, FWHM, and  $\log R'_{HK}$  time series, after the best-fit linear trend is removed. These can be seen on the right panels of Figure 3.

All periodograms show a forest of peaks around 27 days, the synodic rotation period of the Sun ([Wilcox 1972](#)). These peaks are significant (i.e. higher than the 1% false alarm probability) in all four time series. However, in the RVs the most significant peak is at the first harmonic of the rotation period, around 13.5 days. The BIS shows the periodogram structure closest to that of the RVs, also with a significant peak around 13.5 days but with lower power than the 27 days peak. On the contrary, the 13.5 days peak does not appear as significant in the FWHM and  $\log R'_{HK}$  periodograms. At longer periods, all time series show periodogram peaks around 200 days, most noticeable in the activity indicators than in the RVs. This is

probably related to secular trends due to smooth long-term changes in the CCF area ([Collier Cameron et al. 2019](#)).

The periodograms clearly show that both the RVs and the activity indicators contain signals induced by activity, which have different structure in each time series. We note that this periodogram analysis serves just as a data exploratory step, and will only loosely inform our prior assumptions when modelling the data.

### 5.2 Setup for the GPRN analysis

We proceed with the application of the GPRN framework to the solar observations, first modelling the individual time series and then jointly pairing the RVs with each activity indicator. Our aim is to determine whether the GPRN is capable of modelling the RVs jointly with the activity indicators as well as when they are modelled individually. The closer the results, the higher will be the information carried by the given activity indicator about the impact stellar activity has on RVs.

As already mentioned, we will always consider the simplest possible GPRN model, with just one node and thus one weight

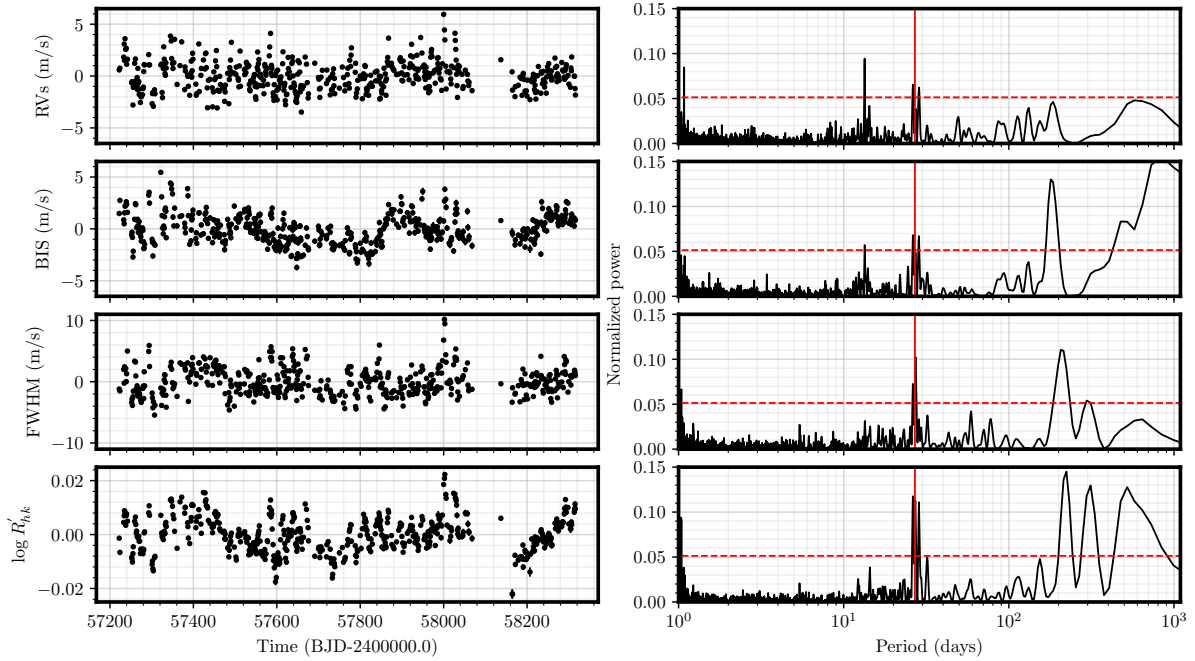


**Figure 3.** The HARPS-N solar telescope RV, BIS, FWHM, and  $\log R'_{HK}$  15-minute averaged measurements we consider in our analysis are displayed on the left after subtracting the best-fit linear trend from the data. The GLS periodograms with respect to these measurements are shown on the right. The vertical solid lines mark the 27-days period, while the horizontal dashed lines show the false alarm probability (FAP) of 1%.

Parameter	Description (units)	Prior
$\eta_1^n$	Amplitude (m/s)	$\mathcal{MLU}([y_{RV}, y_{AI}]_{\sigma}^{\min}, 2[y_{RV}, y_{AI}]_{\text{ptp}}^{\max})$
$\eta_2^n$	Decaying timespan (days)	$\mathcal{LU}(\delta t_{\text{av}}, 10 t_{\text{span}})$
$\eta_3^n$	Period (days)	$\mathcal{U}(10, 50)$
$\eta_4^n$	Length scale	$\mathcal{LU}(0.1, 5)$
$\eta_1^w$	Amplitude (m/s)	$\mathcal{MLU}(y_{\sigma}, 2 y_{\text{ptp}})$
$\eta_2^w$	Decaying timescale (days)	$\mathcal{LU}(\delta t_{\text{av}}, 10 t_{\text{span}})$
s	White noise amplitude (m/s)	$\mathcal{MLU}(y_{\sigma}, 2 y_{\text{ptp}})$
slope	Slope of the mean function (m/s/day)	$\mathcal{N}(0, y_{\sigma}/t_{\sigma})$
offset	Offset of the mean function (m/s)	$\mathcal{U}(y_{\min}, y_{\max})$

**Table 2.** GPRN hyper-parameters and associated prior distributions used in the analysis of the HARPS-N solar observations. The  $y_{RV}$  and  $y_{AI}$  represent, respectively, the observed RVs and activity indicators (FWHM, BIS, or  $\log R'_{HK}$ ), while  $t$  denotes the times of the observations. We denote by  $\delta t_{\text{av}}$  the average time between consecutive observations,  $t_{\text{span}}$  represents the timespan of the observations, while  $y_{\sigma}$  and  $y_{\text{ptp}}$  are the standard deviation and peak-to-peak difference for a given vector of observations  $y$ , respectively.  $\mathcal{U}(a, b)$  stands for a uniform distribution between  $a$  and  $b$ .  $\mathcal{LU}(a, b)$  represents a log-uniform distribution with shape parameters  $a$  and  $b$ .  $\mathcal{MLU}$  denotes the modified log-uniform distribution, a log-uniform distribution whose support includes zero. Note that for the GPRN joint analysis of the RVs and an activity proxy, the  $\eta_1^n$  prior was defined using the smallest  $y_{\sigma}$  and  $y_{\text{ptp}}$  among the two datasets.

per dataset analysed, each having associated hyper-parameters. The node is assumed to have a quasi-periodic covariance function, while each weight has a squared exponential covariance function with specific hyper-parameters. As before, the node and weight hyper-parameters are identified by the superscripts  $n$  and  $w$ , respectively.

The prior distributions used in all analysis are shown in Table 2. Whenever two datasets were jointly analysed the prior for the node amplitude,  $\eta_1$ , was adapted: the knee of the modified log-uniform prior (the point where the distribution changes from uniform to log-uniform) is now defined as the lowest standard deviation of the two

time series, denoted by  $[y_{RV}, y_{AI}]_{\sigma}^{\min}$ . The upper bound of this prior distribution is specified to be twice the largest of the two peak-to-peak amplitudes obtained from the RVs and the activity indicator being considered, and represented by  $[y_{RV}, y_{AI}]_{\text{ptp}}^{\max}$ . The prior for the  $\eta_1$  associated with each weight only uses the standard deviation and peak-to-peak amplitude of the dataset the weight is related to.

The  $\eta_2$  parameters for the node and weights were assigned broad log-uniform priors between the mean time difference between consecutive points,  $\delta t_{\text{av}}$ , and ten times the full timespan of the data,  $t_{\text{span}}$ . In addition, to recover more physically-meaningful values

(see, e.g., Kosiarek & Crossfield 2020), the value for the  $\eta_2$  associated with the node,  $\eta_2^n$ , was a priori constrained to have values higher than half the value of  $\eta_3$ . This also ensures  $\eta_3$  can be interpreted as a period. The weights  $\eta_2$  values,  $\eta_2^w$ , are also assumed a priori to be higher than  $\eta_2^n$ . These conditions ( $0.5 \eta_3 < \eta_2^n < \eta_2^w$ ) should increase the chances the node will model the rotation-induced signals created by active regions, while the weights model their evolution on the longer timescales related to the solar magnetic cycle. Favouring a priori slowly varying weight functions will also reduce the risk of overfitting the data.

A linear mean function was associated to each time series, parameterised by a slope and an offset. For the slope, we assign a Gaussian prior with zero mean and standard deviation equal to the ratio of the standard deviations of the measurements and the timestamps. A uniform prior between the minimum and maximum values of the respective dataset was used for the offset. Finally, each dataset is also associated with a jitter term,  $s$ , which models additional stationary Gaussian white noise not accounted for by the observational uncertainties. Each jitter is assigned a modified log-uniform prior.

Similarly to the analysis of Section 4, we use `emcee` to explore the parameter space. The same setup is used, with the number of walkers equal to twice the number of hyper-parameters, and the same convergence criteria applied as before.

### 5.3 Results

We will first describe the results of the analysis of each dataset individually. The GPRN model used here, with just one node and one weight, approximates a GP in the limit of a constant weight (or a very large  $\eta_2^w$ ). The difference then resides in the shape of the joint posterior with respect to the outputs, which in the GP case is a multivariate Gaussian, while in the GPRN case is generally a multivariate distribution with longer tails. The weight in the GPRN provides some additional flexibility to model non-stationary changes in the solar activity signals over the three years of observations. The results of an analysis with a GPRN with one node and one weight can thus be compared to some extent with those obtained using a GP model (Langellier et al. 2021).

Afterwards, we present the results of the joint analysis of RVs and each of the activity indicators, again assuming only one node in the GPRN. In this case, the node will describe the assumed shared quasi-periodic activity-related latent process.

For each analysis, we quote the *maximum a posteriori* (MAP) value for the joint posterior distribution of the hyper-parameters, as well as the medians and 68% credible intervals (i.e. the 16% and 84% quantiles) with respect to all marginal posterior distributions. These values are shown in Tables 3 and 4. The corner plots showing the marginal, single and pairwise, posterior distributions for all hyper-parameters are in Appendix D. Most of these distributions are well defined and localised. The posterior distributions for the  $\eta_1$  parameters are exceptions, due to the strong anti-correlation between the node and weight values for those parameters, whose product must equal the variance per dataset to a first approximation. Further, the posterior distributions for some weight GP timescales ( $\eta_2^w$ ) are ill-defined for very large values of these parameters, in the sense that they just follow the behaviour of the prior distribution for such values. This is because the data does not contain information that can be used to distinguish between them.

#### 5.3.1 Individual analysis

The analyses of the four datasets individually, using the GPRN model previously described, all lead to similar results for the values of the GPRN hyper-parameters. In particular, we always recover with high precision the synodic rotation period of the Sun, about 27 days, through  $\eta_3^n$ . All the inferred timescales for the decaying rotation-induced correlations,  $\eta_2^n$ , are close, within 19 to 23 days, and consistent taking into account their associated 68% credible intervals. The very high inferred values for the timescales of the weight functions,  $\eta_2^w$ , suggest that the time series behave in a quasi-stationary manner. This can be clearly seen through the slowly varying predictive means for the weights, shown on appendices C1, C2, C3, and C4. Nevertheless, the fact that the weight functions clearly show a decreasing trend, whichever the dataset considered, is an indication of non-stationary behaviour due to diminishing data variance, as expected of a star approaching its activity minimum.

All four GPRN models managed to achieve very good fits to the data, as can be seen in Figure 4. Subtracting the MAP predictive mean from each respective dataset leads to a residual rms significantly lower than that of the original dataset. The RV rms was reduced by a factor of 2.8, from 1.928 m/s to 0.689 m/s. The decrease in the case of the FWHM was similar (by a factor of 2.2), while for the BIS and  $\log R'_{HK}$  we find even higher rms reduction factors of 4.9 and 9.7, respectively. These could indicate some degree of over-fitting, but all the residual rms values are higher than the average measurement uncertainties associated with each dataset, by factors of 5.2 (RVs), 1.5 (BIS), 3.8 (FWHM) and 1.2 ( $\log R'_{HK}$ ). This in fact suggests measurement uncertainties may have been underestimated, systematic effects are present (e.g. due to instrument miscalibration or atmospheric phenomena) and/or there are physical processes occurring in the Sun which are not being modelled adequately by the GPRN, like granulation and super-granulation. The latter change on timescales of a few hours to days (Meunier & Lagrange 2019), significantly smaller than the timescales associated with solar rotation and longer-term magnetic cycles.

In Figure 5 we show the GLS periodograms for the residuals after subtracting from each time series the respective MAP predictive means. The periodograms of the original data (i.e. same as in Figure 3) are also shown for comparison. Clearly, the GPRN model can describe essentially all the power present in the original time series, with no significant peaks left in the periodograms of the residuals. The model de-correlates the data to the point where the residuals resemble white noise.

#### 5.3.2 RV and BIS

The first joint analysis combined the RV and BIS measurements. Figure 6 shows the GPRN posterior predictive means and standard deviations using the MAP values of the hyper-parameters. As expected, the reduction in rms, from the original datasets to the sets of residuals obtained by subtracting the MAP predictive means from the former, is now somewhat lower than the reduction in rms obtained through the analysis of the datasets individually. The RV and BIS rms are now reduced by a factor of 1.6 and 4.7, instead of 2.8 and 4.9, respectively. This results from our imposition of a common latent process behind the generation of the two datasets, whose characteristics are described through the single node. Surprisingly, the node seems to give preference to fitting the BIS over the RV measurements. This can be seen in the significantly smaller degradation in the rms reduction, but also in the much lower increase in

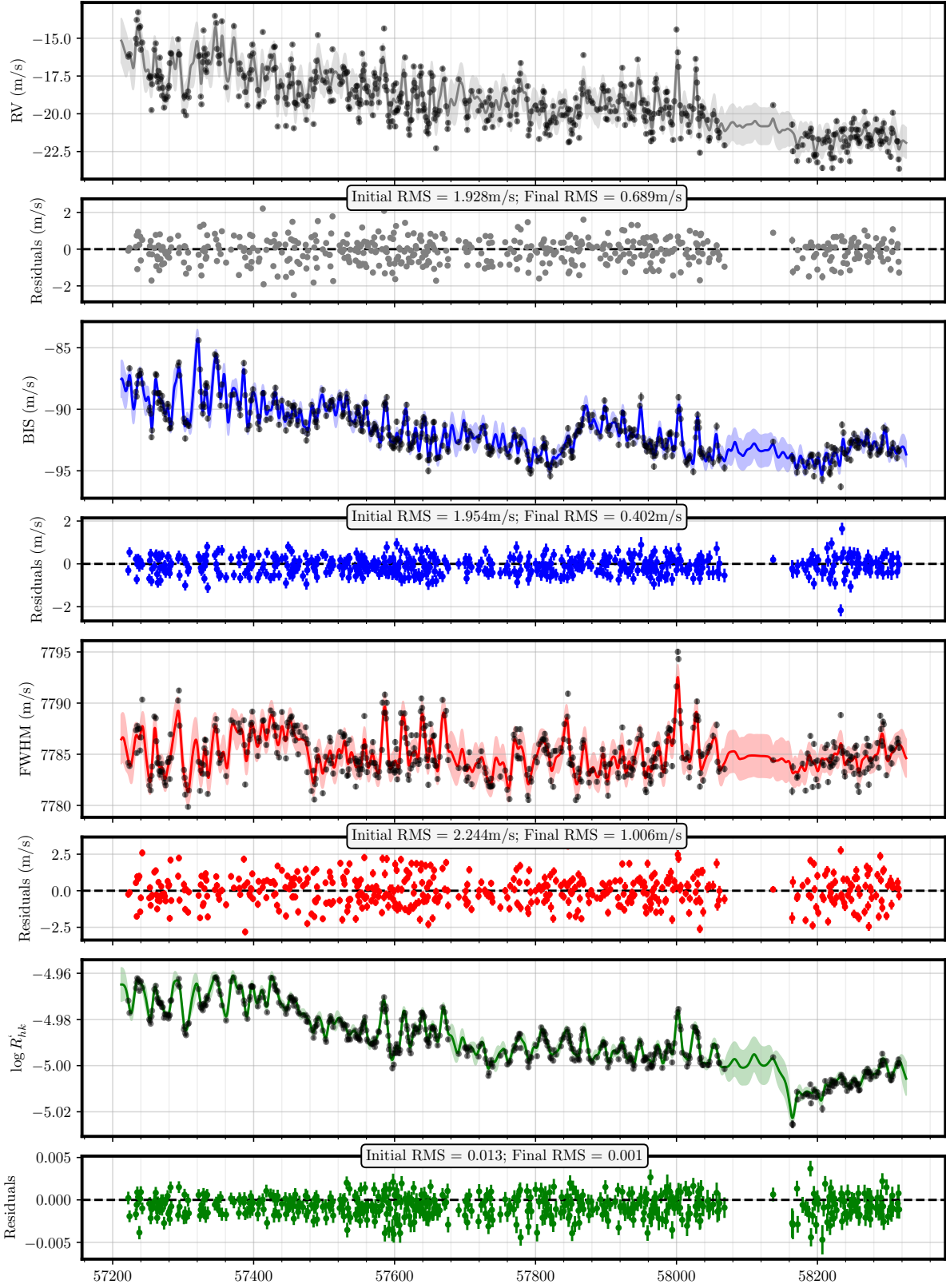


**Figure 4.** Visual representations of the predictive means and standard deviations associated with the MAP values for the GPRN hyper-parameters obtained when each considered time series is analysed individually. The panels show, from top to bottom, the results for the analysis of the RVs (in grey), the BIS (in blue), the FWHM (in red), and the  $\log R'_{HK}$  (in green), as well as the measured values and associated uncertainties (which are not always visible). We also show the residuals after subtracting the predictive means associated with each dataset, and quote the rms associated with the data shown (initial) and with the residuals (final).

Parameter	RV		BIS		FWHM		$\log R'_{HK}$	
	MAP	Median	MAP	Median	MAP	Median	MAP	Median
$\eta_1^n$	0.720	$1^{+5}_{-1}$	1.568	$2^{+5}_{-1}$	0.647	$2^{+6}_{-1}$	0.010	$0.05^{+0.04}_{-0.02}$
$\eta_2^n$ [days]	19.972	$20.3^{+2.0}_{-1.9}$	23.235	$23.6^{+1.6}_{-1.6}$	19.001	$19.1^{+1.6}_{-1.8}$	20.530	$20.5^{+1.4}_{-1.4}$
$\eta_3^n$ [days]	25.921	$26.2^{+0.7}_{-0.6}$	26.853	$27.0^{+0.4}_{-0.4}$	28.244	$28.0^{+0.6}_{-0.6}$	28.273	$27.4^{+0.7}_{-0.7}$
$\eta_4^n$	0.584	$0.61^{+0.07}_{-0.06}$	0.724	$0.73^{+0.06}_{-0.05}$	0.731	$0.72^{+0.09}_{-0.09}$	1.074	$1.05^{+0.09}_{-0.08}$
$\eta_1^w$ [m/s]	1.038	$2^{+5}_{-1}$	0.855	$1^{+5}_{-1}$	1.898	$2^{+6}_{-1}$	0.102	$0.05^{+0.04}_{-0.03}$
$\eta_2^w$ [days]	1001.229	$3569^{+4026}_{-2123}$	2431.229	$4909^{+3589}_{-2517}$	1812.053	$4662^{+3829}_{-2618}$	4124.169	$5519^{+3541}_{-2991}$
s [m/s]	0.781	$0.79^{+0.04}_{-0.04}$	0.414	$0.418^{+0.030}_{-0.030}$	1.136	$1.13^{+0.06}_{-0.06}$	0.001	$0.00100^{+0.00009}_{-0.00008}$

**Table 3.** Results for the GPRN analysis of the datasets individually. The superscripts on some hyper-parameters identify if they belong to the node ( $n$ ) or to the weights ( $w$ ):  $\eta_1^n$ ,  $\eta_2^n$  and  $\eta_3^n$  control, respectively, the amplitude, the decay timescale and the periodicity of the correlations between the node outputs, while  $\eta_4$  defines their timescale of variation relative to  $\eta_3$ ;  $\eta_1^w$  and  $\eta_2^w$  control, respectively, the amplitude and the decay timescale of the correlations between each weight outputs. The first column identifies each hyper-parameter, while each subsequent pair of columns show the MAP values associated with the joint posterior distribution of the GPRN hyper-parameters and the median values plus 16th and 84th percentiles (68% credible intervals) with respect to the marginal posterior distributions of each GPRN hyper-parameter, in the case of the RVs, BIS, FWHM and  $\log R'_{HK}$ , respectively.

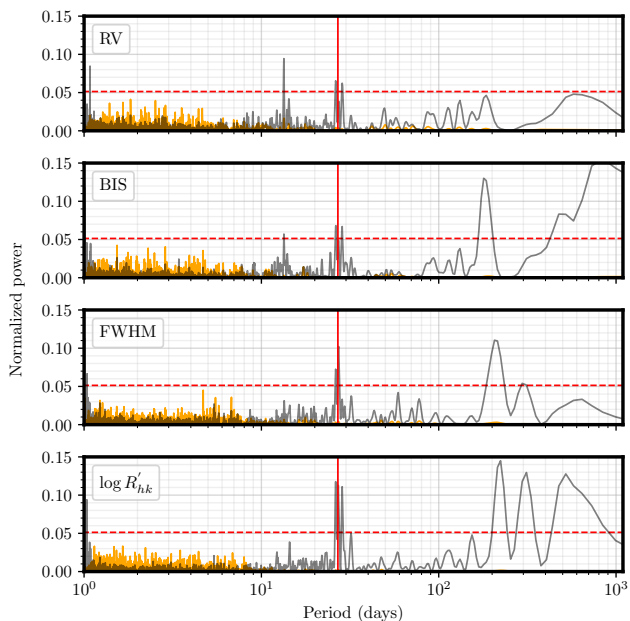


**Figure 5.** Comparison of the GLS periodograms of the time series depicted in Figure 3 (in grey) and of their residuals after subtracting the MAP predictive means derived when each time series is analysed individually with the GPRN model considered (in orange). The vertical solid lines mark the 27-days period, while the horizontal dashed lines show the false alarm probability (FAP) of 1% (all in red).

the MAP value for the jitter, 2% for the BIS versus 52% for the RVs, and in the posterior predictive uncertainties, with respect to what was found in the individual analysis. This could be the result of the somewhat lower harmonic complexity present in the BIS dataset, as can be seen by comparing the BIS and RV periodograms.

The mode for the posterior marginal distribution for  $\eta_3^n$  is very close to 27 days, the synodic rotation period of the Sun, but there are local maxima near 36–37 days and 44–45 days (see Figure D5). These are associated with increasingly smaller values for  $\eta_4^n$ , but do not seem correlated with specific values of the other hyper-parameters.

The estimate for  $\eta_2^n$  is consistent with the average lifetime of active regions being of a few weeks, close to the solar rotation period (e.g. Hathaway & Choudhary 2008; van Driel-Gesztelyi & Green 2015).

As was the case in the individual analysis of the datasets, the posterior predicted means for the weight functions show a decrease during the timespan of the observations. This results from the evolution of the solar magnetic cycle, which was approaching an activity minimum. The clearly more structured weight function in the case of the RVs (see Figure C5) just reflects the need to compensate for the degradation in the quality of the fit provided by the node.

### 5.3.3 RV and FWHM

We now turn our attention to the joint analysis of the RVs and FWHM. Figure 7 shows the GPRN posterior predictive means and standard deviations using the MAP values of the hyper-parameters. As in the previous joint analysis, the reduction in rms, from the original datasets to the sets of residuals obtained by subtracting the MAP predictive means from the former, is lower than the reduction in rms obtained through the analysis of the datasets in isolation. The RV and FWHM rms are reduced by a factor of 1.9 and 2.1, instead of 2.8 and 2.2, respectively. Again, the node gives preference to fitting the activity indicator. This is also reflected in the significantly lower increase in the MAP value for the jitter, 8% for the FWHM versus 38% for the RVs, and in the posterior predictive uncertainties, with respect to what was found in the individual analysis. Lower harmonic complexity in the case of the FWHM may be also behind this preferred behaviour for the GPRN.

We again recover a precise estimate for the synodic rotation period of the Sun, and most of the MAP values for the other hyper-parameters are similar to what was previously found in the joint analysis of RVs and BIS. The largest difference is in the behaviour of the weight connecting the node to the RV dataset, which prefers a significantly smaller timescale  $\eta_2^w$ . In Figure C6 it can be seen that indeed the preferred RV weight function has noticeably more structure, besides a general downwards trend.

As before, the preference of the node for fitting more closely the variations observed in the activity indicator leaves to the weight function the task of compensating for the node function in order to match the RV variations. But it seems unlikely that the considerable complexity of the RV weight function is explained solely by

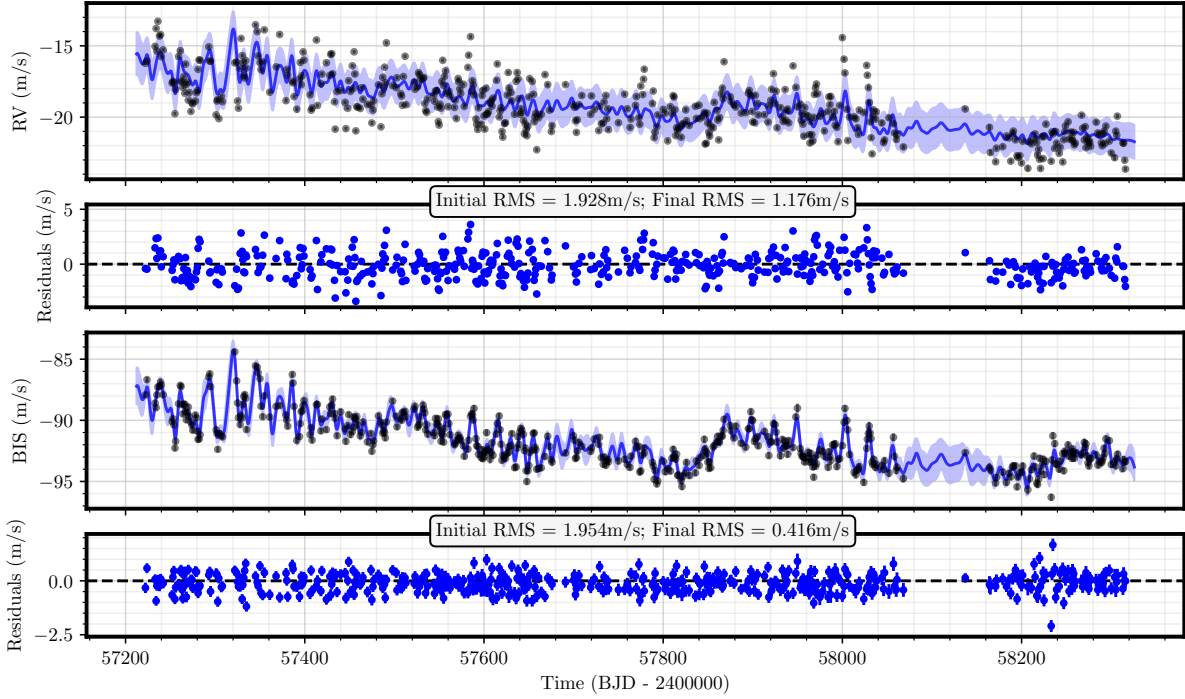


**Figure 6.** Predictive means and standard deviations associated with the MAP values for the GPRN hyper-parameters obtained when the RVs and BIS are analysed jointly. Measured values, residuals (after subtracting the respective predictive means) and associated uncertainties (which are not always visible) are also shown, as well as the rms associated with the (initial) data and with the (final) residuals.

Parameter	RV and BIS		RV and FWHM		RV and $\log R'_{HK}$	
	MAP	Median	MAP	Median	MAP	Median
$\eta_1^n$	1.163	$0.5^{+1.4}_{-0.4}$	1.951	$0.51^{+1.15}_{-0.34}$	0.001	$0.07^{+0.05}_{-0.03}$
$\eta_2^n$ [days]	24.319	$23.6^{+1.6}_{-1.6}$	22.183	$20.8^{+1.9}_{-2.0}$	19.654	$20.5^{+1.4}_{-1.4}$
$\eta_3^n$ [days]	26.745	$27.1^{+0.4}_{-0.4}$	27.643	$27.7^{+0.6}_{-0.6}$	28.615	$28.3^{+0.7}_{-0.7}$
$\eta_4^n$	0.783	$0.74^{+0.06}_{-0.06}$	1.008	$0.86^{+0.12}_{-0.11}$	1.057	$1.08^{+0.09}_{-0.08}$
RV $\eta_1^w$ [m/s]	0.413	$2^{+5}_{-2}$	0.440	$2^{+4}_{-1}$	5.939	$10^{+6}_{-4}$
RV $\eta_2^w$ [days]	281.890	$2058^{+4117}_{-1677}$	37.319	$66^{+56}_{-24}$	86.682	$89^{+22}_{-19}$
AI $\eta_1^w$ [m/s]	0.669	$3^{+7}_{-2}$	0.675	$5^{+9}_{-3}$	0.024	$0.06^{+0.04}_{-0.03}$
AI $\eta_2^w$ [days]	1676.794	$5074^{+3661}_{-2669}$	1660.697	$4674^{+3920}_{-2729}$	3041.504	$5898^{+3313}_{-3012}$
RV $s$ [m/s]	1.187	$1.20^{+0.04}_{-0.04}$	1.074	$1.129^{+0.056}_{-0.006}$	1.126	$1.12^{+0.04}_{-0.04}$
AI $s$ [m/s]	0.423	$0.438^{+0.032}_{-0.030}$	1.229	$1.20^{+0.06}_{-0.06}$	0.001	$0.00100^{+0.00009}_{-0.00009}$

**Table 4.** As in Table 3, but with respect to the GPRN joint analysis of the datasets, from left to right, RVs and BIS, RVs and FWHM, RVs and  $\log R'_{HK}$ .

this effect. This suggests that the RVs and FWHM do not share a common latent activity process to the extent that was observed for the RVs and BIS, at least when such process is assumed to have a quasi-periodic structure.

### 5.3.4 RV and $\log R'_{HK}$

The final joint analysis considers the RV and  $\log R'_{HK}$  datasets. The GPRN posterior predictive means and standard deviations, using the MAP values of the hyper-parameters, are shown in Figure 8. Contrary to the previous cases, the quality of the MAP fit to the activity indicator does not show any degradation with respect to

the MAP fit obtained for the  $\log R'_{HK}$  dataset individually. But the MAP fit to the RVs shows the typical reduction in rms improvement when moving from the individual to the joint analysis, decreasing from a factor of 2.8 to about 1.7.

The  $\log R'_{HK}$  periodogram resembles best what one would expect from a quasi-periodic process centred around a dominant (stellar rotation) period (see Figure 3), as assumed in the set-up of the GPRN. Thus, it should not be surprising that the joint analysis leads to a preferred model configuration where the node essentially fits the  $\log R'_{HK}$ , leaving for the RV weight (for which the  $\eta_2^w$  MAP is again relatively small, around 88 days) the onus of adapting the node output to match the RV dataset (see Figure C7).

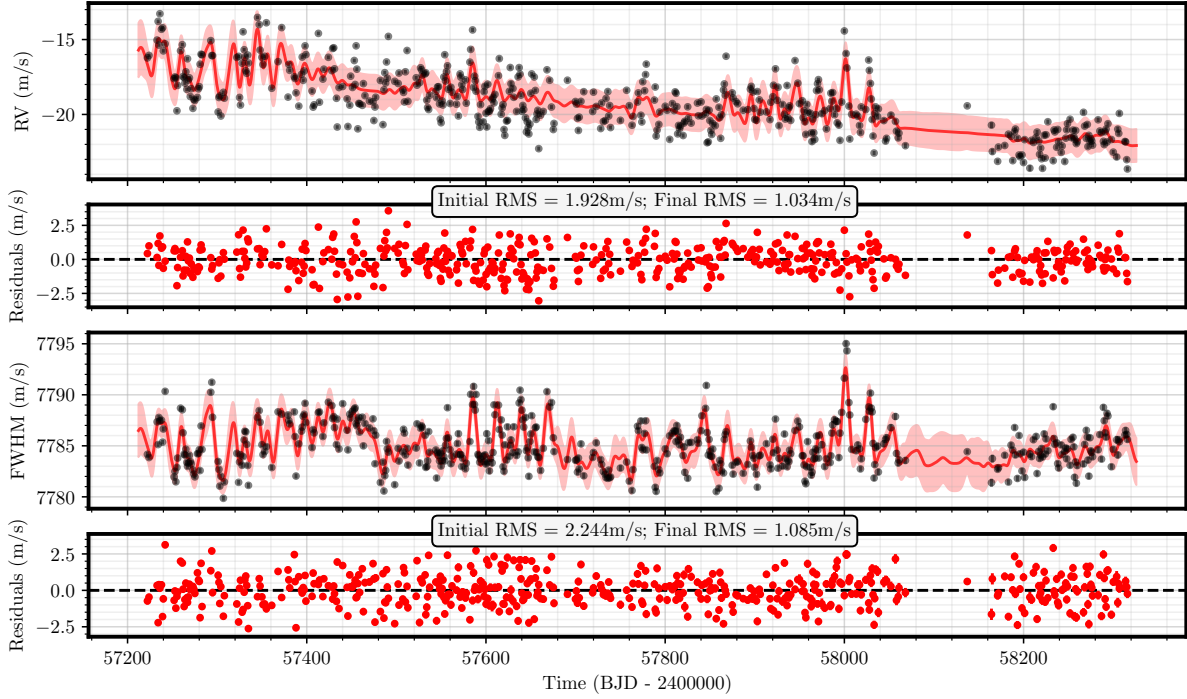


**Figure 7.** As in Figure 6, but with respect to the joint analysis of the RVs and FWHM datasets.

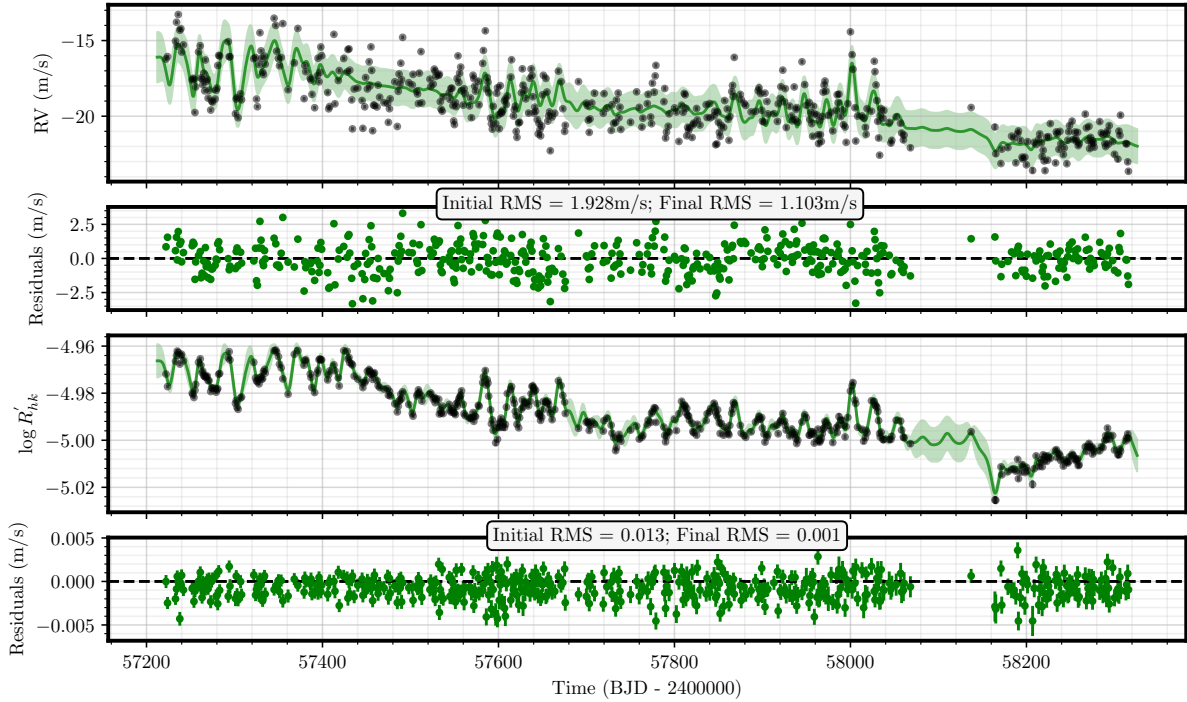


**Figure 8.** As in Figure 6, but with respect to the joint analysis of the RVs and  $\log R'_{HK}$  datasets.

#### 5.4 Interpretation of the results

We have already seen that we can recover the synodic solar rotation period when the time series are analysed both individually and jointly. In fact, overall the MAP values obtained for the GPRN hyper-parameters in all analyses are very similar (see Tables 3 and

4). This suggests the RVs and activity indicators share the same type of temporal evolution.

The GPRN model we considered is able to describe very well the behaviour of each time series individually, leading to substantial reductions in rms and in the significance of periodogram peaks when

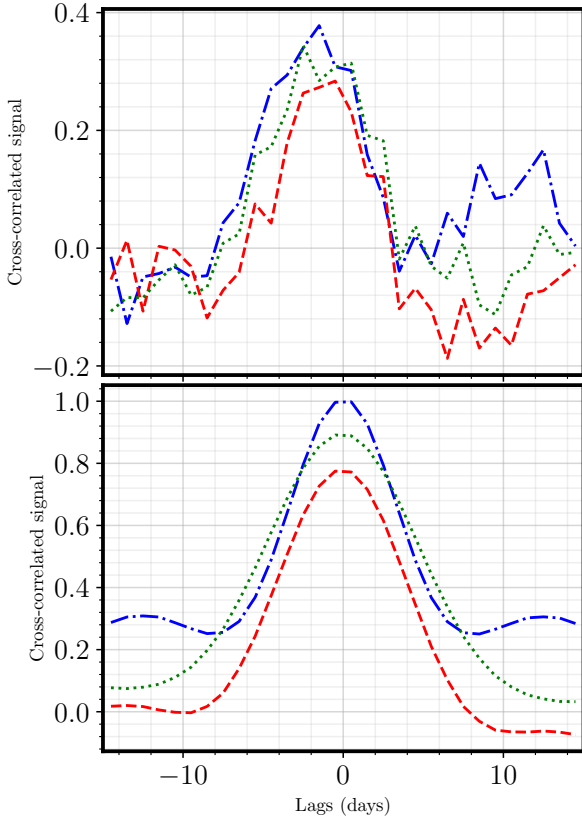


**Figure 9.** Cross-correlation functions (CCFs) between the RVs and activity indicators - BIS (in blue), FWHM (in red) and  $\log R'_{HK}$  (in green). The upper panel shows the CCFs between the observed time series, while the lower panel shows the CCFs between the MAP predictive means at the observed timestamps, obtained through the joint analysis of the measured RVs plus the given activity indicator.

the MAP predictive means are subtracted from the original datasets (see Figure 5). However, such reductions are significantly smaller for the RVs when this dataset is analysed jointly with an activity indicator. A degradation in the quality of the best-fit solutions was expected to some extent given that in the joint analysis we are forcing the node to model two independently acquired datasets. Nevertheless, the magnitude of such degradation in the case of the RVs is surprising given how close the MAP values obtained for the GPRN hyper-parameters are for all individual analysis. One possible cause for this may be the presence of temporal delays between the solar RVs and activity indicators, which the GPRN model, with only one node, should find very difficult to reproduce.

Indeed, time lags of 1 and 3 days between the RVs and the FWHM and BIS measurements, respectively, were identified by Collier Cameron et al. (2019). Since the datasets we consider differ somewhat from the ones they assembled (see section 5), we used the algorithm developed by Edelson & Krolik (1988) to determine the discrete correlation function between the RVs and activity indicators, in search for possible temporal delays in our datasets. The results are shown in the upper panel of Figure 9, and suggest that the RVs lead all activity indicators by 1 to 2 days. As expected, the MAP predictive means of the RVs and activity indicators obtained in the joint analysis do not show any sign of such time lags, as can be seen through their correlation functions in the lower panel of Figure 9. The failure to model this aspect of the cross-correlation

between the time series should lead to worse fits when they are jointly modelled, as found.

Finally, both the individual and joint analysis of the time series lead to preferred posterior predicted means for the weight functions that decrease over the timespan of the observations. This implies an overall decrease in the variances of the time series, correctly reproducing the expected diminishing solar activity as the Sun approached the minimum of its 11-years sunspot cycle. Thus, the detection and characterisation of the non-stationary behaviour of the activity indicators does not seem to be much impacted by the inability of the one-node GPRN to model the time lag between the RVs and activity indicators.

## 6 DISCUSSION AND CONCLUSIONS

We have presented a new framework to model RV observations in combination with activity indicators. A GPRN combines  $Q$  nodes and  $Q \times P$  weights to model  $P$  time series, with all nodes and weights defined as independent GPs. This makes it possible to model non-stationary outputs, an improvement with respect to currently existing frameworks.

We tested our GPRN implementation on simulated datasets, and demonstrated its capabilities on real Sun-as-a-star observations obtained with the HARPS-N spectrograph. We obtained physically sensible values for the GPRN hyper-parameters, recovering for example the synodic solar rotation period, both when the time series were analysed individually and jointly.

The joint analysis of the RVs and an activity indicator leads to a significantly worse description of the RV variations with time than when the RVs are analysed in isolation. This is unfortunate, because such joint analysis may help disentangle better the RV components due to stellar activity and orbiting planets. However, we only considered the simplest possible configuration for a GPRN, with just one node. The inclusion of extra nodes would help in modelling more complex behaviour, in particular that which is not shared by the outputs being analysed.

Previous work by Rajpaul et al. (2015) and Gilbertson et al. (2020), for example, proposed to use a linear combination of a GP and its derivatives to model the RV variations induced by spots, due to their dependence on both the spot coverage of the stellar surface and the suppression of convective blueshift in magnetised regions. Purportedly, the BIS shares the same dependencies as the RVs, but the FWHM and  $\log R'_{HK}$  would be sensitive only to the fraction of the stellar surface covered by spots and, as such, would not require the use of the derivative term. Our results seem to lend some support to this hypothesis, given that the node by itself seems to be able to describe better the RVs jointly with the BIS than with either the FWHM or the  $\log R'_{HK}$ . This can be perceived through the significantly higher complexity required for the weight function associated with the RVs in the later cases (cf. Figure C5 with Figures C6 and C7).

On the other hand, the MAP fit to the RVs when modelled jointly with the BIS leads to a worse residual rms than what is obtained in the other joint analyses. These contradicting results could be due to the seemingly larger time lag between the RVs and the BIS than with respect to the other activity indicators (see Figure 9). This behaviour is difficult to model by the weight associated with the RVs and could justify the worse residual rms when the RVs are analysed jointly with the BIS as well as push such weight towards the adoption of a simpler form.

The joint analysis of the RVs and an activity indicator could

thus benefit from the inclusion of a second node in the GPRN with a kernel that is the derivative of the kernel assumed for the first node. In particular, if the later is periodic or quasi-periodic, the association of that kernel derivative with a second node would allow for the modelling of any time lag that may exist between the outputs. However, such feature could eventually be also modelled directly, through the introduction of  $P - 1$  lag parameters, one per output, while keeping just one node.

Nevertheless, if the main objective is to use the information in activity indicators to constrain the behaviour of the RV component induced by stellar activity, care must be taken not to increase the flexibility of the GPRN to the point where it could model RVs and activity indicator(s) almost independently. While the probability of this happening increases with the number of nodes assumed, it can be mitigated to some extent by not allowing the number of hyper-parameters to grow proportionally.

Another aspect that we would like to study in the future pertains to the type and combination of kernels used in the nodes and weights, including the introduction of non-stationary white noise. In particular, we cannot exclude the possibility that our choice of a squared exponential kernel for the weights limits too much the extent to which the node output can be modified. Although widely used, this kernel is known to be too smooth to realistically model a considerable number of physical processes (e.g. Stein 1999).

Interestingly, although the simple GPRN model we considered seems unable to fully model RVs and activity indicators jointly, it is still capable of describing the RVs well enough for the rms to be reduced by a factor of 1.6 to 1.9 (1.93 m/s  $\rightarrow$  1.18 - 1.03 m/s) when the MAP predictive means are subtracted from the RV measurements. These are higher rms reduction factors than what has been previously reported for HARPS-N solar RVs in the published literature. For example, Langellier et al. (2021) achieved a rms reduction factor of 1.4, from 1.65 m/s to 1.14 m/s, by analysing HARPS-N solar RVs with a GP where all the quasi-periodic kernel hyper-parameters, except the amplitude, were fixed a priori to the MAP values obtained through a previous GP-based analysis of the HARPS-N solar S-index data. The same rms reduction factor was also obtained by Collier Cameron et al. (2021), from 1.76 m/s to 1.25 m/s, and Milbourne et al. (2019), from 1.65 m/s to 1.21 m/s, using very different methodologies. Although some of the rms reduction factors mentioned above were obtained without taking into account a linear trend, our results are almost unchanged when we do not include such a trend in the mean function of the GPRN. Further, given that the GPRN posterior predictive distribution has heavier-tails than a Gaussian, the quality of the best-fit GPRN model to the HARPS-N solar data may actually be better than what is suggested by the residual rms.

Ultimately, the usefulness of the methods that have been proposed to help disentangle the RV contributions due to stellar activity and orbiting planets will have to be tested and compared using data for stars other than the Sun. The inclusion of Keplerians in the mean function associated with the RVs is the only change required in the GPRN framework we presented for it to be ready for such purpose.

## ACKNOWLEDGEMENTS

We thank Nuno C. Santos for the many valuable discussions and continuous support during the development of this work. This work was supported by FCT, Fundação para a Ciência e a Tecnologia, through national funds and by FEDER through COMPETE2020, Programa Operacional Competitividade e Internacionalização, by

the following grants: UID/FIS/04434/2019; UIDB/04434/2020; UIDP/04434/2020; PTDC/FIS-AST/32113/2017 and POCI-01-0145-FEDER-032113; PTDC/FIS-AST/28953/2017 and POCI-01-0145-FEDER-028953; PTDC/FIS-AST/28987/2017 and POCI-01-0145-FEDER-028987; PTDC/FIS-AST/30389/2017 and POCI-01-0145-FEDER-030389; EXPL/FIS-AST/0615/2021. J.P.F. is supported in the form of a work contract funded by national funds through FCT with reference DL57/2016/CP1364/CT0005.

## DATA AVAILABILITY

The data and software used in this article are publicly available online in `gpyrn` GitHub repository<sup>3</sup>.

## References

- Aigrain S., Pont F., Zucker S., 2012, *MNRAS*, **419**, 3147  
 Arfken G., Weber H., Harris F., 2013, *Mathematical Methods for Physicists: A Comprehensive Guide*. Elsevier Science  
 Astropy Collaboration et al., 2018, *AJ*, **156**, 123  
 Baliunas S. L., et al., 1995, *ApJ*, **438**, 269  
 Barragán O., Gandolfi D., Antoniciello G., 2019a, *MNRAS*, **482**, 1017  
 Barragán O., et al., 2019b, *MNRAS*, **490**, 698  
 Barragán O., Aigrain S., Rajpaul V. M., Zicher N., 2021, *MNRAS*, **509**, 866  
 Bazot M., Bouchy F., Kjeldsen H., Charpinet S., Laymand M., Vauclair S., 2007, *A&A*, **470**, 295  
 Blei D. M., Kucukelbir A., McAuliffe J. D., 2017, *Journal of the American Statistical Association*, **112**, 859  
 Cegla H. M., et al., 2012, *MNRAS*, **421**, L54  
 Charbonneau P., 2014, *ARA&A*, **52**, 251  
 Cloutier R., et al., 2019, *A&A*, **621**, A49  
 Collier Cameron A., et al., 2019, *MNRAS*, **487**, 1082  
 Collier Cameron A., et al., 2021, *MNRAS*, **505**, 1699  
 Cui G., Yu X., Iommelli S., Kong L., 2016, *IEEE Signal Processing Letters*, **23**, 1662  
 Del Zanna G., Mason H., 2013, in *Planets, Stars and Stellar Systems: Volume 4: Stellar Structure and Evolution*. Springer Netherlands, Dordrecht, pp 87–205  
 Delisle J. B., Unger N., Hara N. C., Ségransan D., 2022, *A&A*, **659**, A182  
 Demin S. A., Nefedyev Y. A., Andreev A. O., Demina N. Y., Timashev S. F., 2018, *Advances in Space Research*, **61**, 639  
 Dumusque X., Udry S., Lovis C., Santos N. C., Monteiro M. J. P. F. G., 2011, *A&A*, **525**, A140  
 Dumusque X., et al., 2015, *ApJ*, **814**, L21  
 Dumusque X., et al., 2021, *A&A*, **648**, A103  
 Edelson R. A., Krolik J. H., 1988, *ApJ*, **333**, 646  
 Faria J. P., Haywood R. D., Brewer B. J., Figueira P., Oshagh M., Santerne A., Santos N. C., 2016, *A&A*, **588**, A31  
 Figueira P., et al., 2010, *A&A*, **513**, L8  
 Figueira P., Santos N. C., Pepe F., Lovis C., Nardetto N., 2013, *A&A*, **557**, A93  
 Foreman-Mackey D., Agol E., Ambikasaran S., Angus R., 2017, *AJ*, **154**, 220  
 Foreman-Mackey D., et al., 2019, *JOSS*, **4**, 1864  
 Gilbertson C., Ford E. B., Jones D. E., Stenning D. C., 2020, *ApJ*, **905**, 155  
 Gomes da Silva J., Santos N. C., Bonfils X., Delfosse X., Forveille T., Udry S., Dumusque X., Lovis C., 2012, *A&A*, **541**, A9  
 Gregory P. C., 2005, *ApJ*, **631**, 1198  
 Guinan E. F., Engle S. G., Durbin A., 2016, *ApJ*, **821**, 81  
 Hathaway D. H., 2015, *Living Reviews in Solar Physics*, **12**, 4  
 Hathaway D. H., Choudhary D. P., 2008, *Sol. Phys.*, **250**, 269  
 Haywood R. D., et al., 2014, *MNRAS*, **443**, 2517

<sup>3</sup> <https://github.com/iastro-pt/gpyrn>

- Heinonen M., Mannerström H., Rousu J., Kaski S., Lähdesmäki H., 2016, in Gretton A., Robert C. C., eds, Proceedings of Machine Learning Research Vol. 51, Proceedings of the 19th International Conference on Artificial Intelligence and Statistics. PMLR, Cadiz, Spain, pp 732–740
- Jones D. E., Stenning D. C., Ford E. B., Wolpert R. L., Loredo T. J., Dumusque X., 2017, preprint (arXiv:1711.01318)
- Jordan M. I., Ghahramani Z., Jaakkola T. S., Saul L. K., 1999, Machine learning, 37, 183
- Karamanis M., Beutler F., Peacock J. A., 2021, *MNRAS*, 508, 3589
- Kjeldsen H., et al., 2008, *ApJ*, 682, 1370
- Kosiarek M. R., Crossfield I. J. M., 2020, *AJ*, 159, 271
- Kullback S., 1959, Information Theory and Statistics. Wiley, New York
- Lagrange A. M., Desort M., Meunier N., 2010, *A&A*, 512, A38
- Langellier N., et al., 2021, *AJ*, 161, 287
- Li S., Xing W., Kirby R. M., Zhe S., 2020, in Proceedings of the Twenty-Ninth International Joint Conference on Artificial Intelligence, IJCAI-20. International Joint Conferences on Artificial Intelligence Organization, pp 2456–2462
- Mayo A. W., et al., 2019, *AJ*, 158, 165
- Mayor M., Queloz D., 1995, *Nature*, 378, 355
- Meunier N., Lagrange A. M., 2019, *A&A*, 625, L6
- Milbourne T. W., et al., 2019, *ApJ*, 874, 107
- Murray I., Adams R. P., MacKay D. J. C., 2010, in The Proceedings of the 13th International Conference on Artificial Intelligence and Statistics. pp 541–548
- Nguyen T. V., 2015, PhD thesis, Australian National University, Research School of Computer Science
- Nguyen T., Bonilla E., 2013, in Proceedings of the Sixteenth International Conference on Artificial Intelligence and Statistics. PMLR, Scottsdale, Arizona, USA, pp 472–480
- Pagano I., 2013, in Planets, Stars and Stellar Systems: Volume 4: Stellar Structure and Evolution. Springer Netherlands, Dordrecht, pp 485–557
- Pepe F., et al., 2021, *A&A*, 645, A96
- Petersburg R. R., et al., 2020, *AJ*, 159, 187
- Plagemann C., Kersting K., Burgard W., 2008, in Machine Learning and Knowledge Discovery in Databases. Springer Berlin Heidelberg, Berlin, Heidelberg, pp 204–219
- Quadrianto N., Kersting K., Xu Z., 2010, in Encyclopedia of Machine Learning. Springer US, Boston, MA, pp 428–439
- Rajpaul V. M., 2017, PhD thesis, University of Oxford
- Rajpaul V., Aigrain S., Osborne M. A., Reece S., Roberts S., 2015, *MNRAS*, 452, 2269
- Rasmussen C. E., Williams C. K. I., 2006, Gaussian Processes for Machine Learning. MIT Press
- Robertson P., Mahadevan S., Endl M., Roy A., 2014, *Science*, 345, 440
- Saar S. H., Donahue R. A., 1997, *ApJ*, 485, 319
- Santos N. C., Gomes da Silva J., Lovis C., Melo C., 2010, *A&A*, 511, A54
- Santos N. C., et al., 2014, *A&A*, 566, A35
- Schrijver C. J., Zwaan C., 2000, Solar and Stellar Magnetic Activity. Cambridge Astrophysics. Cambridge University Press
- Sokal A., 1997, in Functional Integration: Basics and Applications. Springer US, Boston, MA, pp 131–192
- Speagle J. S., 2020, *MNRAS*, 493, 3132
- Stein M. L., 1999, Interpolation of Spatial Data. Springer New York
- Styan G. P., 1973, *Linear Algebra and its Applications*, 6, 217
- Wilcox J. M., 1972, in Cosmic Plasma Physics. Springer US, Boston, MA, pp 157–164
- Wilson A. G., 2014, PhD thesis, University of Cambridge
- Wilson A. G., Knowles D. A., Ghahramani Z., 2012, in Proceedings of the 29th International Conference on Artificial Intelligence and Statistics. PMLR, Cadiz, Spain, pp 1139–1146
- Zechmeister M., Kürster M., 2009, *A&A*, 496, 577
- van Driel-Gesztelyi L., Green L. M., 2015, *Living Reviews in Solar Physics*, 12, 1

## APPENDIX A: UPDATES FOR VARIATIONAL MEANS AND COVARIANCES

Closed-form updates for the variational parameters can be obtained from mean-field theory (Nguyen & Bonilla 2013; Nguyen 2015). For the nodes, the variational means and covariances are given by

$$\begin{aligned} \mu_{f_i} &= \Sigma_{f_j} \sum_{i=1}^P \sum_{j=1}^Q \frac{1}{\sigma_{y_i}^2} \left( \mathbf{y}_i - \sum_{k \neq j} \mu_{w_{ik}} \circ \mu_{f_k} \right) \circ \mu_{w_{ij}} \\ \Sigma_{f_j} &= \left[ K_{f_j}^{-1} + \sum_{i=1}^P \frac{1}{\sigma_{y_i}^2} \text{diag} \left( \mu_{w_{ij}} \circ \mu_{w_{ij}} + \text{diag} \left( \Sigma_{w_{ij}} \right) \right) \right]^{-1} \end{aligned} \quad (\text{A1})$$

while for each weight they are given by

$$\begin{aligned} \mu_{w_{ij}} &= \Sigma_{w_{ij}} \sum_{i=1}^P \sum_{j=1}^Q \frac{1}{\sigma_{y_i}^2} \left( \mathbf{y}_i - \sum_{k \neq j} \mu_{f_k} \circ \mu_{w_{ik}} \right) \circ \mu_{f_j} \\ \Sigma_{w_{ij}} &= \left[ K_{w_{ij}}^{-1} + \sum_{i=1}^P \frac{1}{\sigma_{y_i}^2} \text{diag} \left( \mu_{f_j} \circ \mu_{f_j} + \text{diag} \left( \Sigma_{f_j} \right) \right) \right]^{-1}. \end{aligned} \quad (\text{A2})$$

In these equations,  $\sigma_i$  is calculated following equation 6,  $\mathbf{y}_i$  is the vector containing the measurements from dataset  $i$ ,  $K$  is the covariance matrix for the respective node or weight, while  $\text{diag}$  and  $\circ$  represent the matrix diagonal and the Hadamard product (e.g. Styan 1973), respectively.

## APPENDIX B: EVIDENCE LOWER BOUND

The ELBO of a GPRN model can be divided in three terms, as in equation (9). The first, known as the expected log-likelihood, is given by

$$\begin{aligned} \mathbb{E}_q [\log p(D|\mathbf{f}, \mathbf{w})] &= -\frac{1}{2} \sum_{n=1}^N \sum_{i=1}^P \left[ \log 2\pi \left( \sigma_{y_{err_{ni}}}^2 + \sigma_{y_i}^2 \right) \right] \\ &\quad - \frac{1}{2\sigma^2} \sum_{n=1}^N \left( \mathbf{y}_n^T - \mathcal{W}_{w_n} \mathcal{F}_{f_n} \right)^T \left( \mathbf{y}_n^T - \mathcal{W}_{w_n} \mathcal{F}_{f_n} \right) \\ &\quad - \frac{1}{2\sigma^2} \sum_{i=1}^P \sum_{j=1}^Q \left[ \text{diag} \left( \Sigma_{f_j} \right)^T \left( \mu_{w_{ij}} \circ \mu_{w_{ij}} \right) \right. \\ &\quad \left. + \text{diag} \left( \Sigma_{w_{ij}} \right)^T \left( \mu_{f_j} \circ \mu_{f_j} \right) + \text{tr} \left( \Sigma_{f_j} \Sigma_{w_{ij}} \right) \right], \end{aligned} \quad (\text{B1})$$

where  $\text{tr}$  represents the trace of the matrix,  $\mathbf{y}_n^T$  is a  $1 \times P$  vector containing all observations at entry  $n$ ,  $\mathcal{W}_{w_n}$  is a  $P \times Q$  matrix containing the variational means  $\mu_w$  at entry  $n$ , and  $\mathcal{F}_{f_n}$  is a  $P \times 1$  vector containing the variational means  $\mu_f$  at entry  $n$ .

The second term, the expected log-prior, is

$$\begin{aligned} \mathbb{E}_q [\log p(\mathbf{f}, \mathbf{w})] &= -\frac{1}{2} NQ (P+1) \log 2\pi \\ &\quad - \frac{1}{2} \sum_{j=1}^Q \left[ \log |K_{f_j}| + \mu_{f_j}^T K_{f_j}^{-1} \mu_{f_j} + \text{tr} \left( K_{f_j}^{-1} \Sigma_{f_j} \right) \right] \\ &\quad - \frac{1}{2} \sum_{i=1}^P \sum_{j=1}^Q \left[ \log |K_{w_{ij}}| + \mu_{w_{ij}}^T K_{w_{ij}}^{-1} \mu_{w_{ij}} + \text{tr} \left( K_{w_{ij}}^{-1} \Sigma_{w_{ij}} \right) \right], \end{aligned} \quad (\text{B2})$$

where  $K$  is the covariance matrix of the respective node or weight.

The last term is the entropy of the  $q(\mathbf{f}, \mathbf{w})$  distribution and can be calculated with

$$\begin{aligned} \mathcal{H}_q[q(\mathbf{f}, \mathbf{W})] &= \frac{1}{2}NQ(P+1)(1+\log 2\pi) \\ &+ \frac{1}{2} \sum_{j=1}^Q [\log |\Sigma_{f_j}|] + \frac{1}{2} \sum_{i=1}^P \sum_{j=1}^Q [\log |\Sigma_{w_{ij}}|]. \end{aligned} \tag{B3}$$

### APPENDIX C: SOLAR DATA ANALYSIS - POSTERIOR PREDICTIVES

The posterior predictive means and standard deviations for the individual and joint analyses of each time series, as described in section 5, are shown here. The full predictive means and its different components (mean, node and weight functions) are shown separately in the left and right panels of the following figures, respectively.

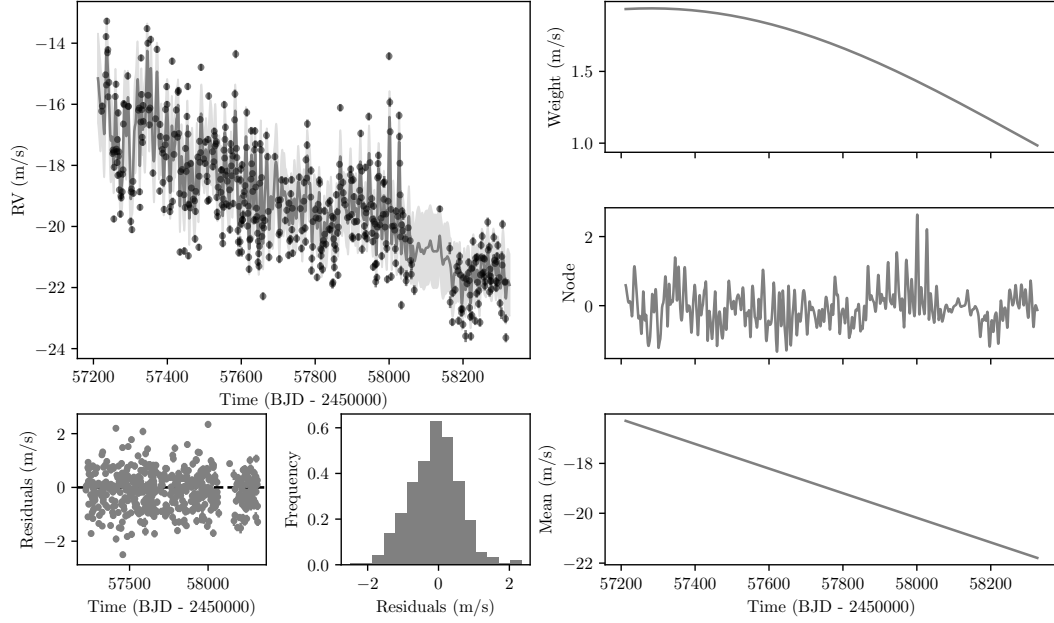


**Figure C1.** On the top-left we show the RV data, as well as the predictive means and standard deviations associated with the MAP values for the GPRN hyper-parameters obtained when the RVs are analysed individually, while on the bottom-left we show the residuals of the data with respect to the predictive means and their histogram distribution. On the right we plot, from top to bottom, the weight, node, and mean functions that contribute to the predictive means.

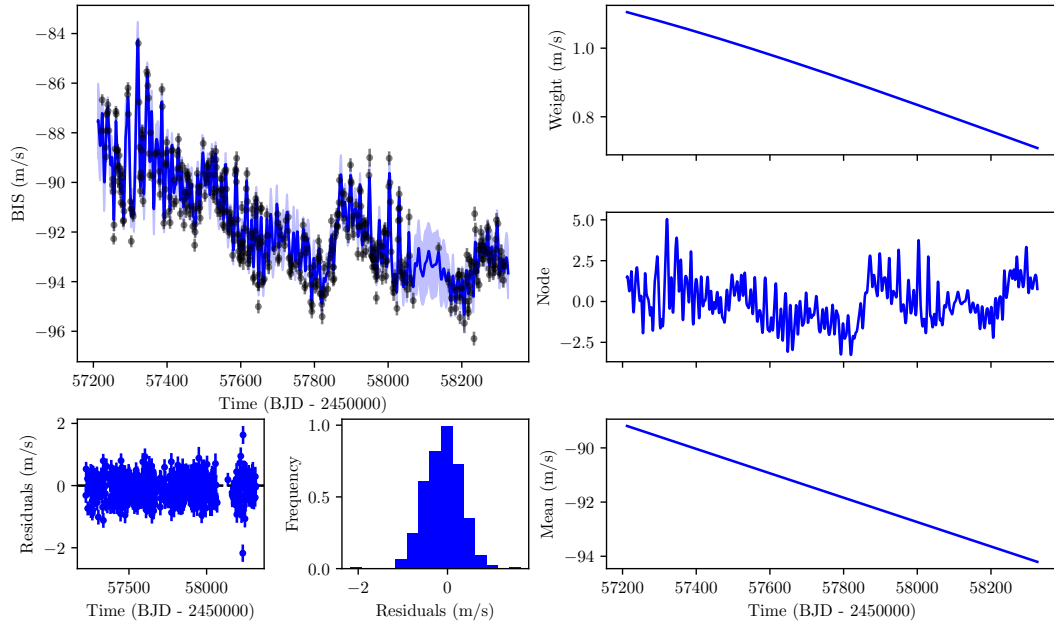


**Figure C2.** As in figure C1, but with respect to the individual analysis of the BIS data.

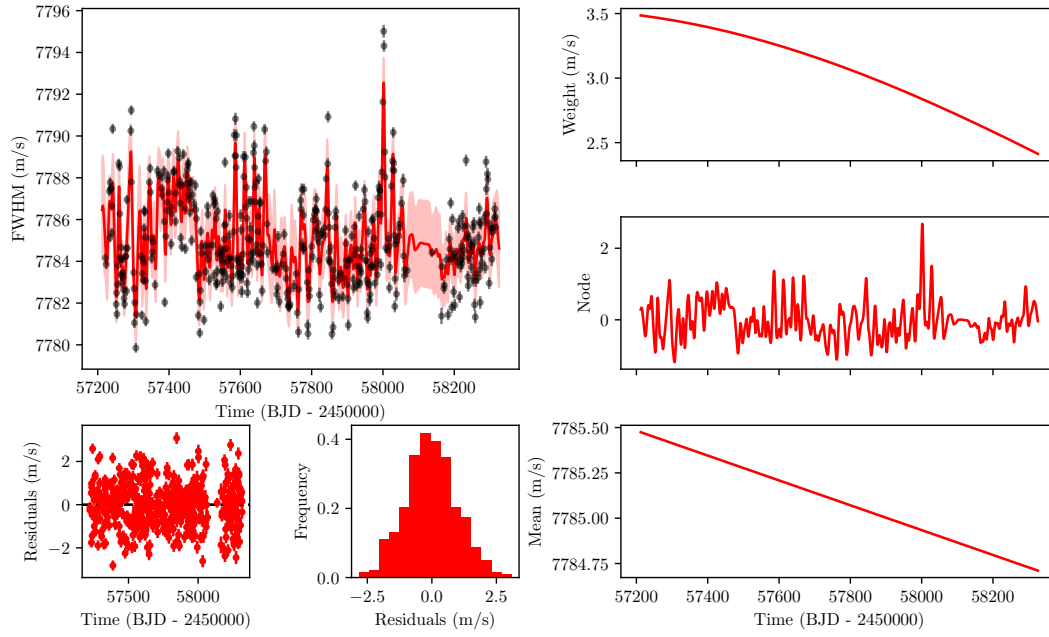


**Figure C3.** As in figure C1, but with respect to the individual analysis of the FWHM data.

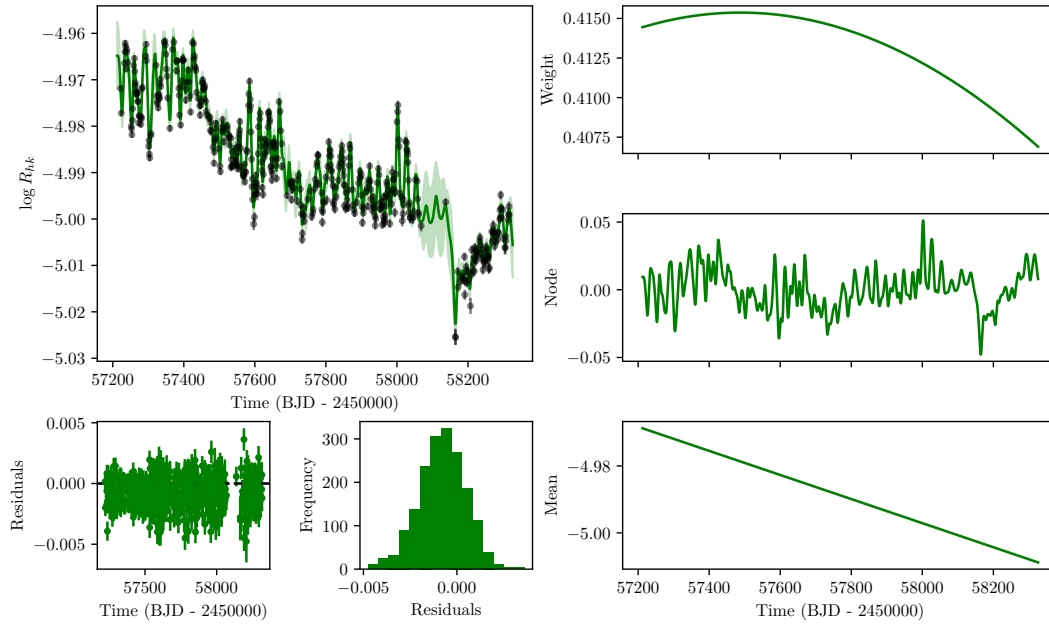


**Figure C4.** As in figure C1, but with respect to the individual analysis of the  $\log R'_{HK}$  data.

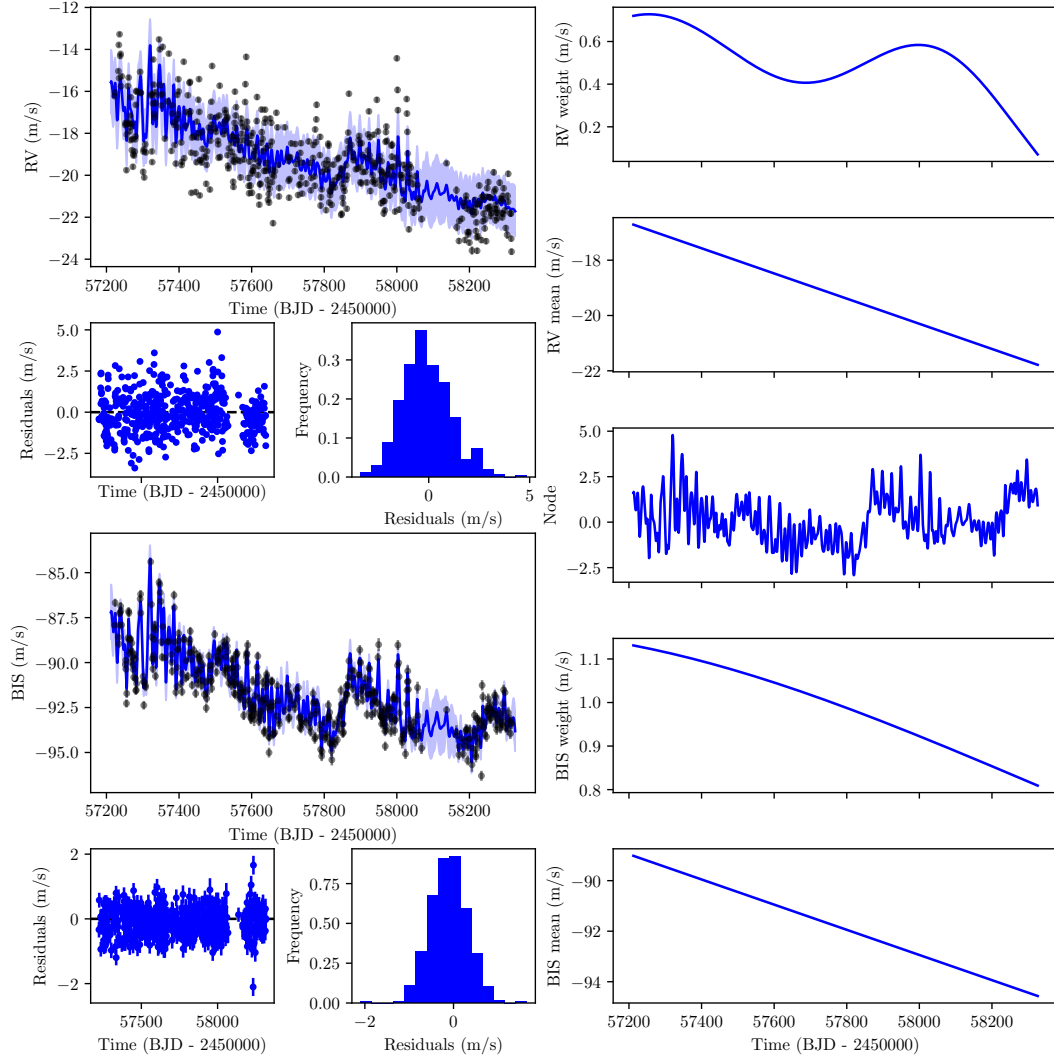


**Figure C5.** On the left we show the RV (top) and BIS (bottom) data, as well as the predictive means and standard deviations associated with the MAP values for the GPRN hyper-parameters obtained when the RVs and BIS are analysed jointly. Below each of those panels we show the respective residuals of the data with respect to the predictive means and their histogram distribution. On the right we show the contribution to the predictive means due to the mean and weight functions for the RVs and BIS, as well as the common node function in the middle.

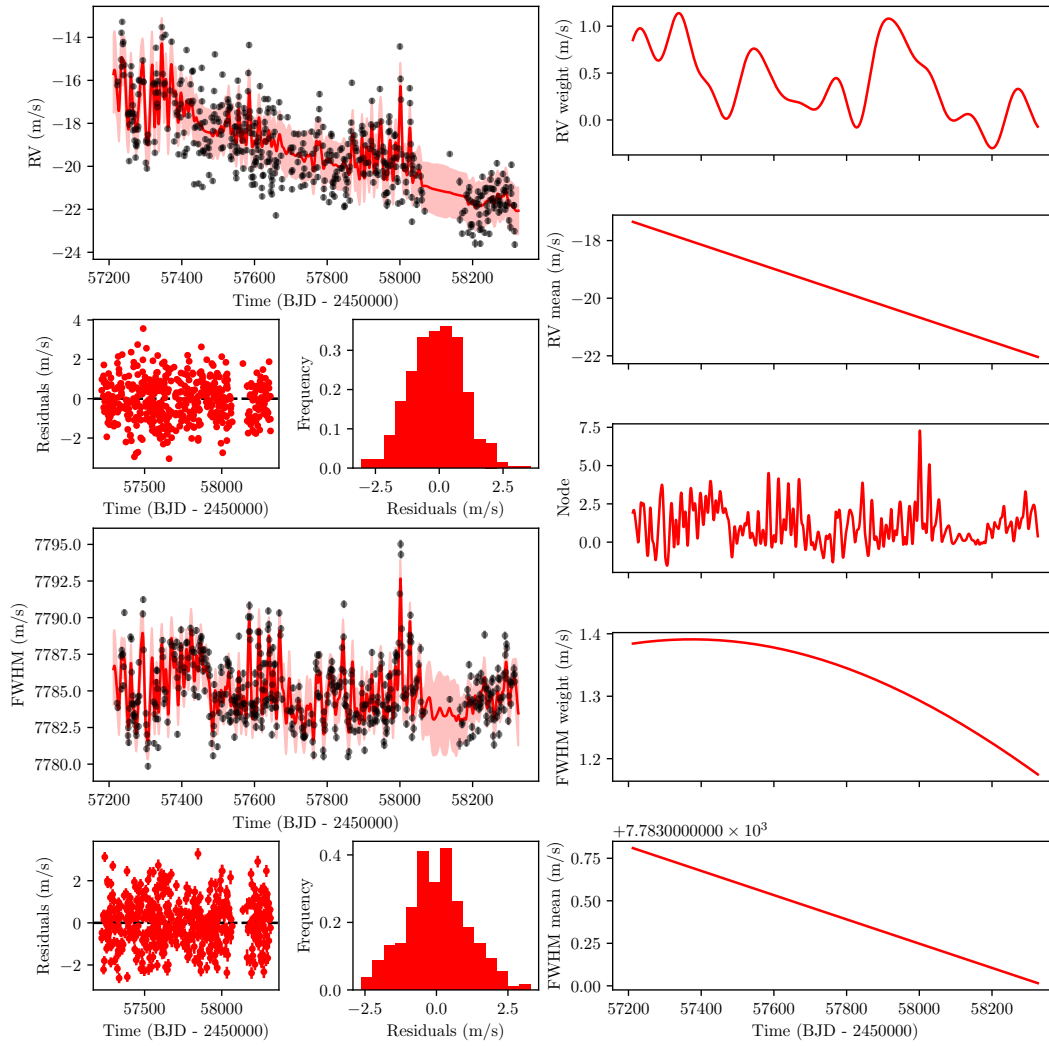


**Figure C6.** As in figure C5, but with respect to the joint analysis of the RV and FWHM data.

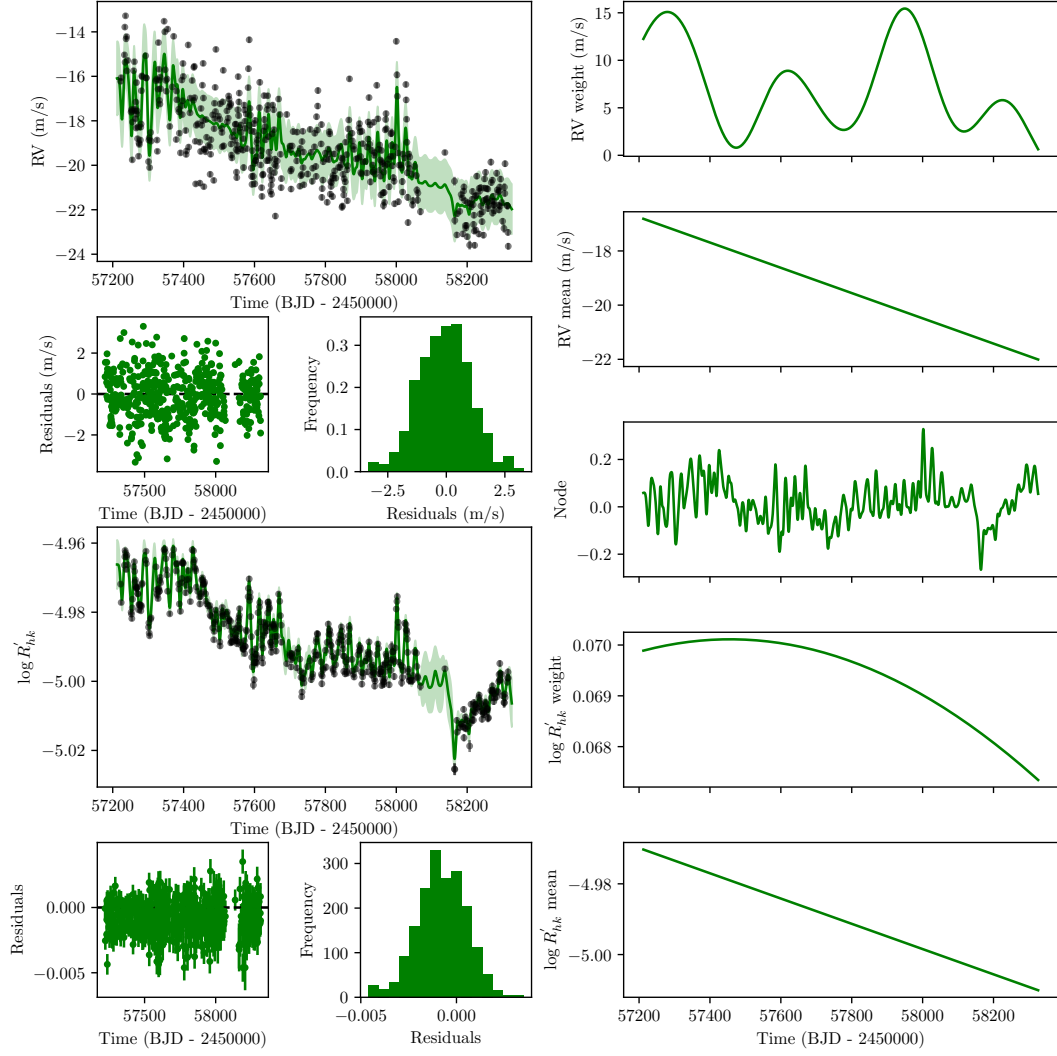
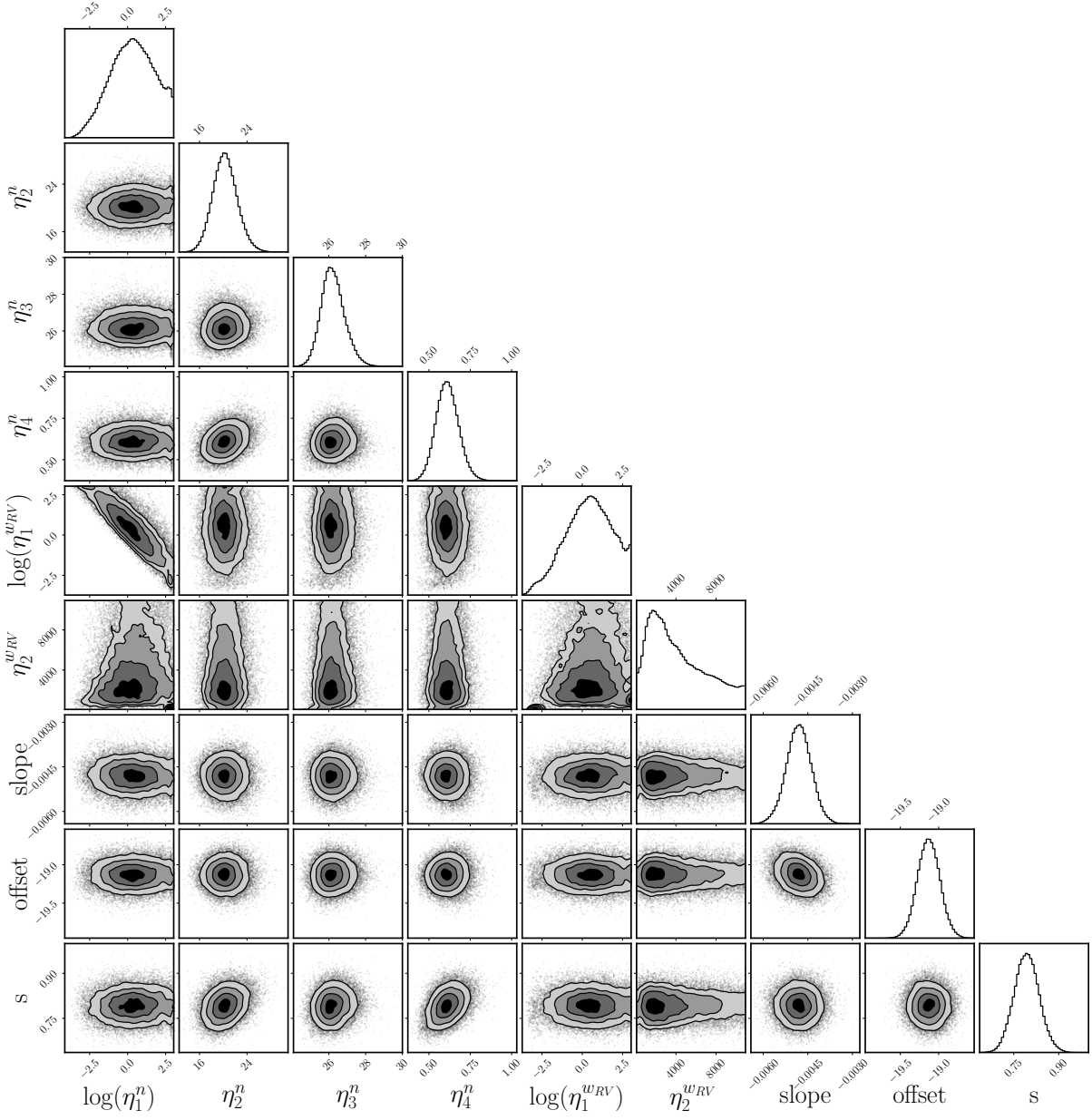


Figure C7. As in figure C5, but with respect to the joint analysis of the RV and  $\log R'_{hk}$  data.

**APPENDIX D: SOLAR DATA ANALYSIS - MARGINAL  
POSTERIOR DISTRIBUTIONS**

The corner plots with the marginal, single and pairwise, posterior distributions obtained for all analyses of the HARPS-N solar data are shown here.



**Figure D1.** Corner plots showing the marginal, single and pairwise, posterior distributions for all GPRN hyper-parameters obtained when the RVs are analysed individually. In order to facilitate the visualization all  $\eta_1$ -type amplitudes are plotted in logarithmic form.

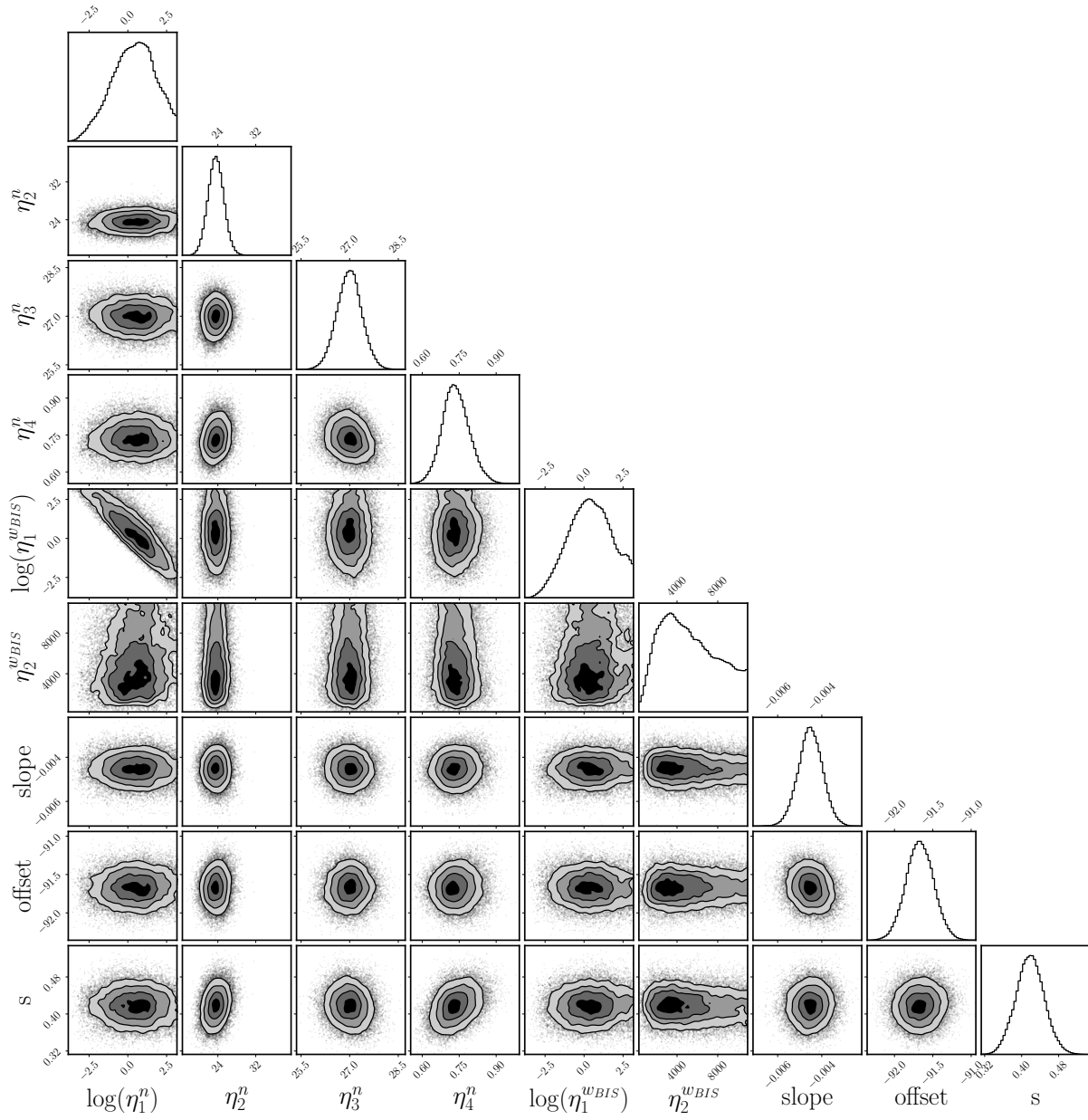


**Figure D2.** As in figure D1, but with respect to the individual analysis of the BIS data.

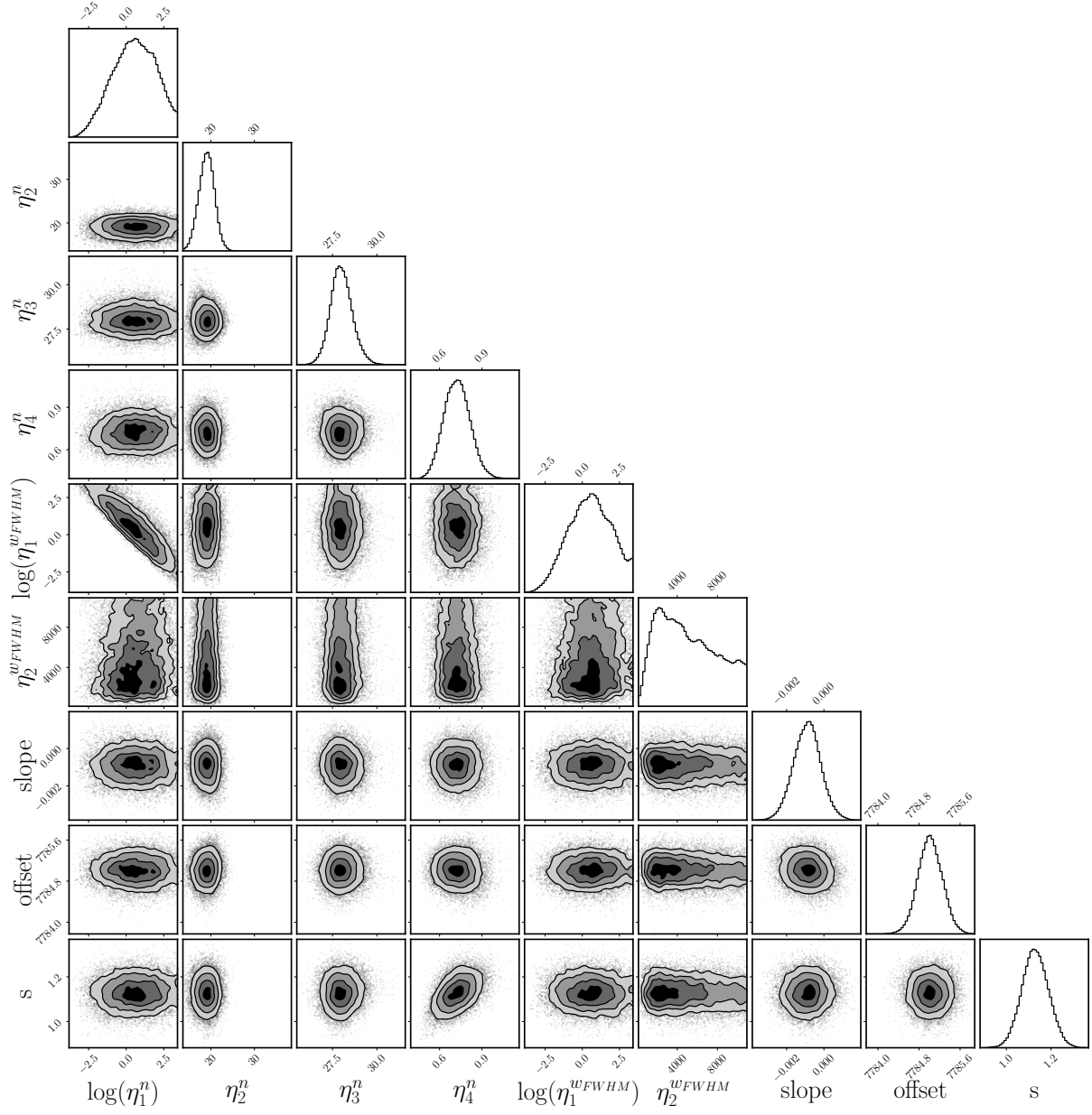


**Figure D3.** As in figure D1, but with respect to the individual analysis of the FWHM data.

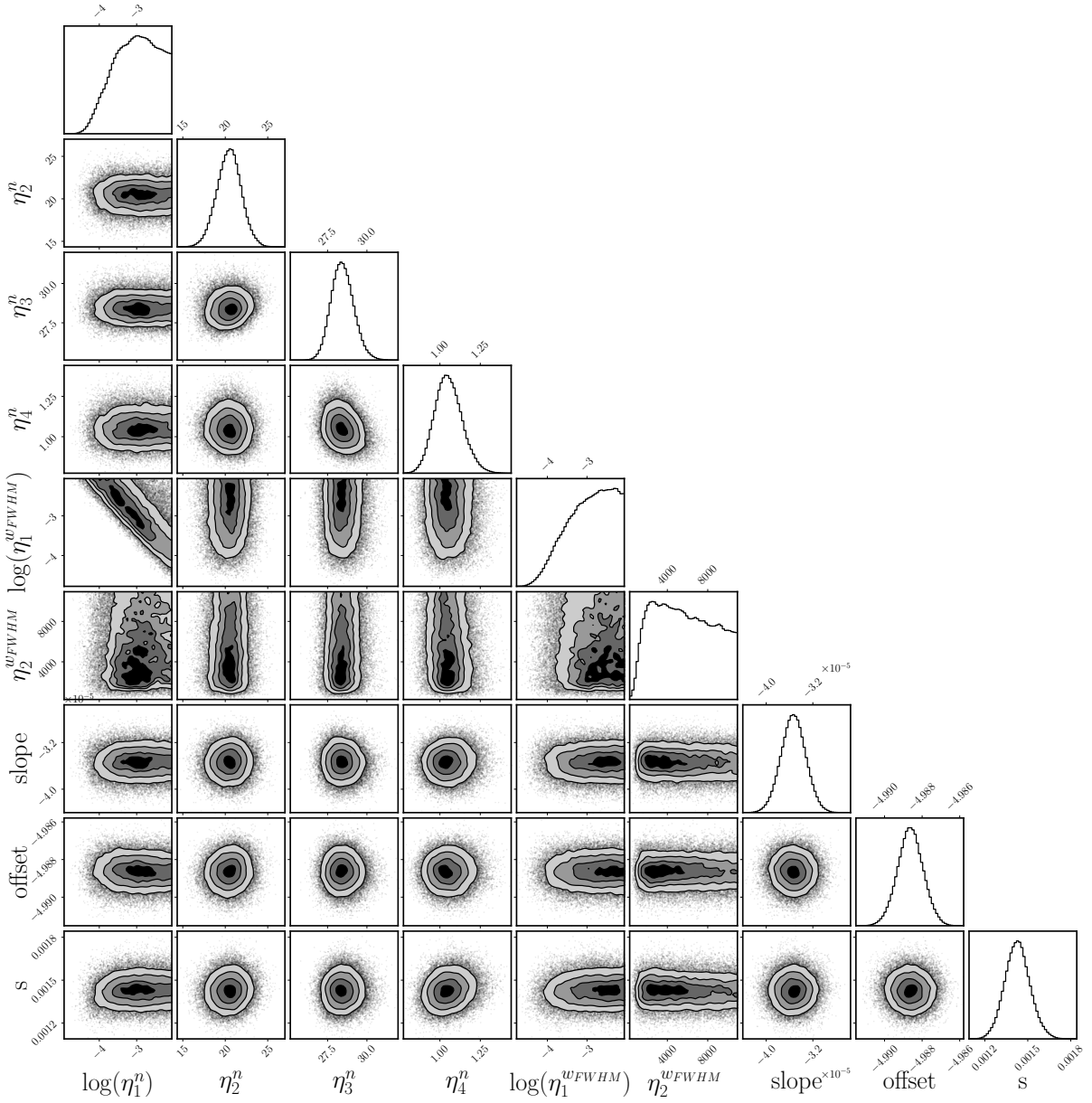


**Figure D4.** As in figure D1, but with respect to the individual analysis of the  $\log R'_{HK}$  data.

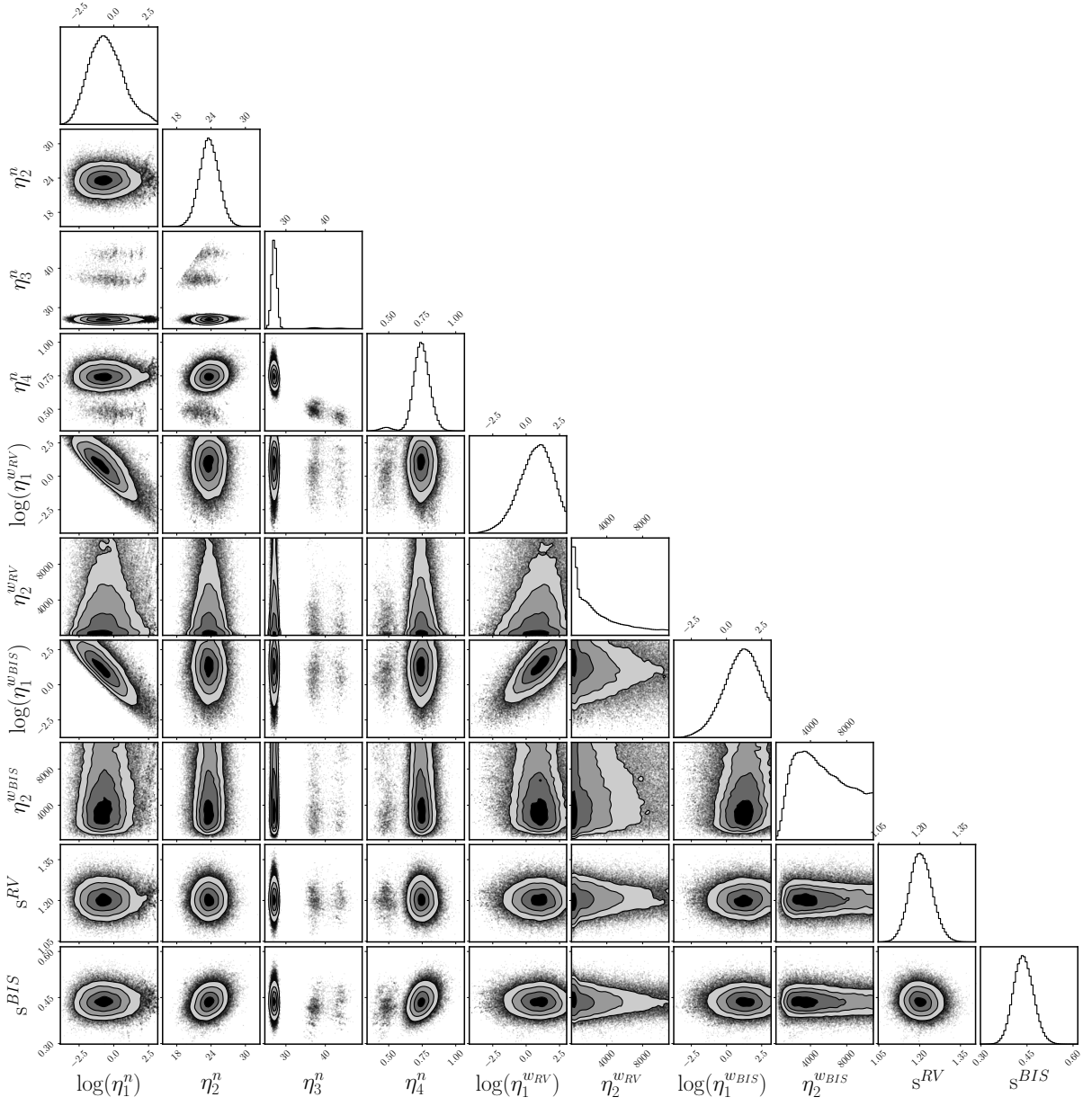


**Figure D5.** Corner plots showing the marginal, single and pairwise, posterior distributions for all GPRN hyper-parameters obtained when the RVs and BIS are analysed jointly. In order to facilitate the visualization all  $\eta_1$ -type amplitudes are plotted in logarithmic form.

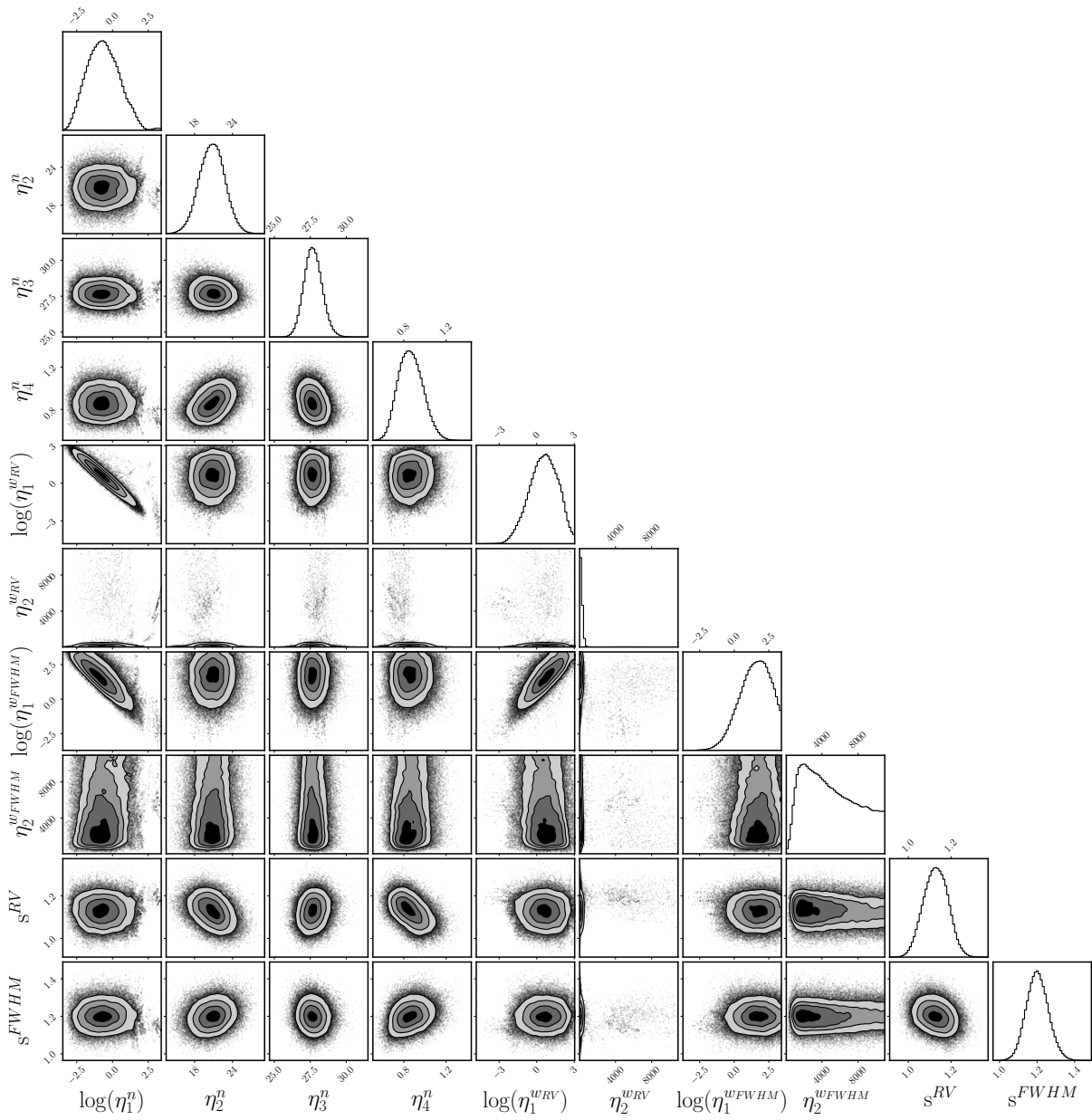


**Figure D6.** As in figure D5, but with respect to the joint analysis of the RV and FWHM data.

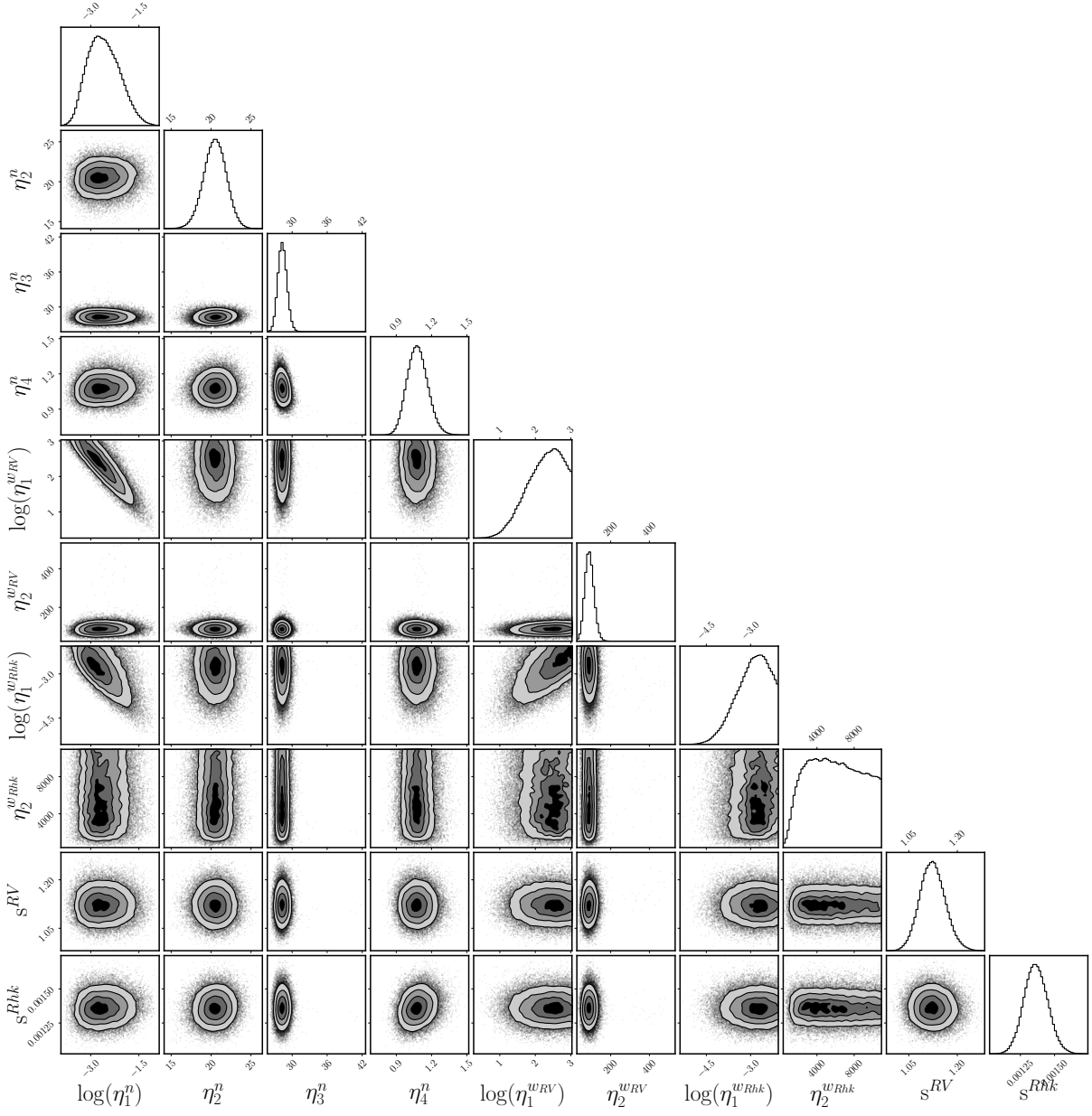


**Figure D7.** As in figure D5, but with respect to the joint analysis of the RV and  $\log R'_{HK}$  data.

This paper has been typeset from a  $\text{\TeX}/\text{\LaTeX}$  file prepared by the author.